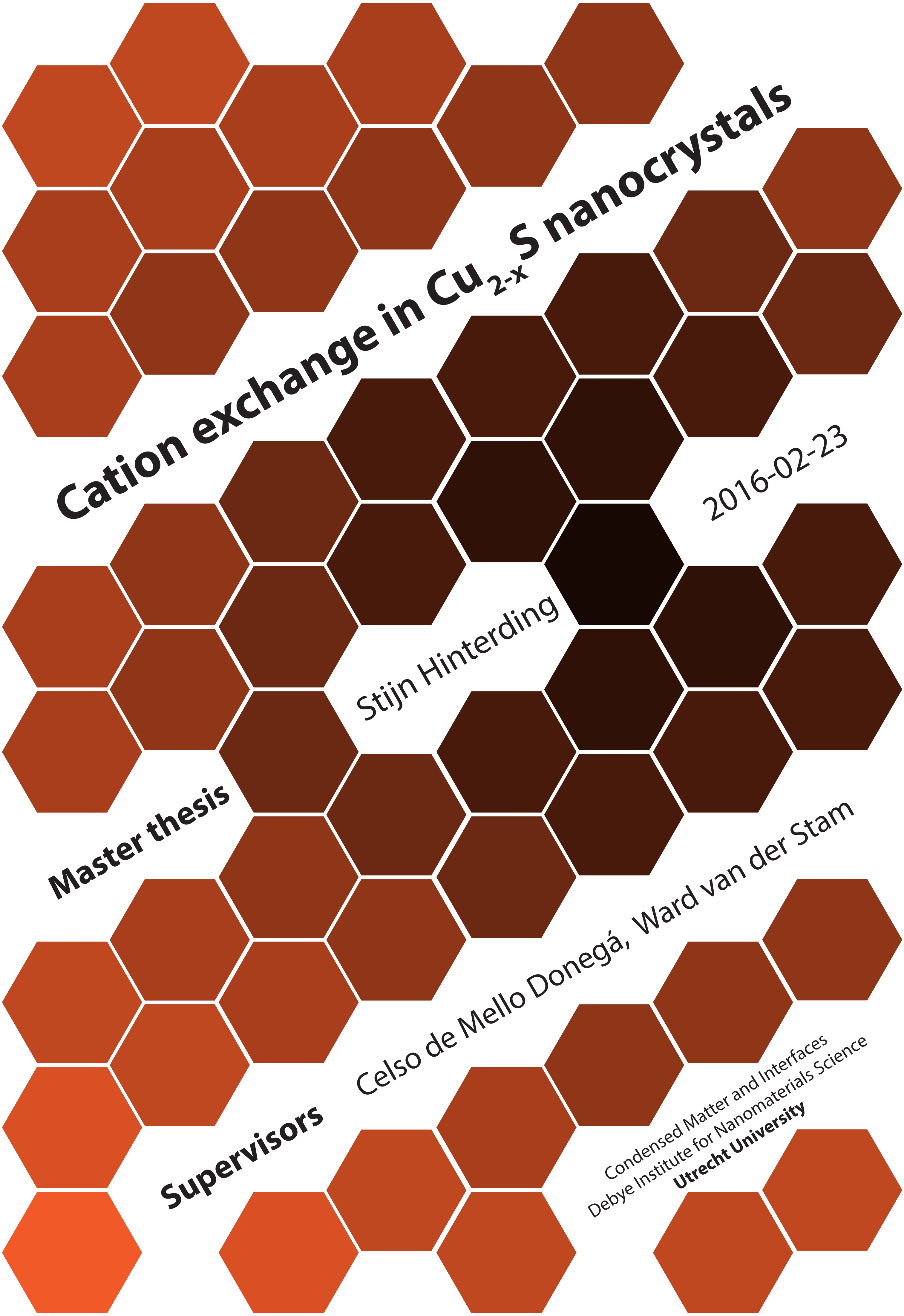

Cation exchange in $Cu_{2-x}S$ nanocrystals

2016-02-23

Stijn Hinterding

Master thesis

Supervisors Celso de Mello Donegá, Ward van der Stam

Condensed Matter and Interfaces
Debye Institute for Nanomaterials Science
Utrecht University

Abstract

Cation exchange reactions allow for control over the composition of semiconductor nanocrystals, while retaining the size, shape and crystal structure of the parent particles. This makes it possible to produce nanocrystals with a combination of size, shape, composition and crystal structure not possible via direct synthesis. A better understanding of the underlying principles of cation exchange may help to successfully exchange cations which cannot be exchanged using existing methods. The use of a single-step cation exchange precursor in heterovalent cation exchange reactions is a recent development, which aims to ease the execution of these reactions. In this work, the cation exchange of Cu^+ for Ga^{3+} in $Cu_{2-x}S$ nanocrystals, using a $GaCl_3$-phosphine complex as Ga-precursor, is studied. Direct adaptation of an existing cation exchange procedure, which converts $Cu_{2-x}S$ into $CuInS_2$, does not lead to successful exchange in $Cu_{2-x}S$ bifrustum nanocrystals. Tuning the reactivity of the $GaCl_3$-phosphine complex, by complexing $GaCl_3$ with diphenyl phosphine and triphenyl phosphite, does allow for successful cation exchange of Cu^+ for Ga^{3+} in these nanocrystals, as indicated by energy-dispersive X-ray spectroscopy (EDX) and selected-area electron diffraction (SAED) measurements . The proposed explanation for this increase in precursor reactivity is based on the electron-withdrawing nature of the precursor side groups. The side groups in diphenyl phosphine and triphenyl phosphite withdraw electron density from the phosphorous atom, which is inferred to weaken the Ga-P bond, resulting in a higher reactivity. Applying the original method, at a higher reaction temperature, to $Cu_{2-x}S$ bipyramid particles does lead to partial heterogeneous cation exchange of Cu^+ for Ga^{3+}. This is evidenced by transmission electron microscopy (TEM), X-ray diffraction (XRD) and EDX measurements. The successful exchange in these particles is attributed to the reactivity of the tips of these particles and/or the higher reaction temperature. The formation of heteronanostructured product nanocrystals is thought to occur, because the diffusion rate of Ga^{3+} in $Cu_{2-x}S$ is too low to fully exchange the nanocrystals. Use of $GaCl_3$ without any additional ligands leads to hollowing of $Cu_{2-x}S$ bifrustum nanocrystals. A study of the progression of the reaction over time, with TEM and high-angle annular dark-field scanning transmission electron microscopy (HAADF-STEM) tomography, suggests that hollowing is due to the formation of a cavity at the nanocrystal surface, which grows inward over time. Elemental mapping using EDX is in agreement with this finding. After longer reaction times, the amount of gallium measured in the nanocrystals increases. Elemental mapping shows that the elemental composition of these particles is heterogeneous, with a Ga-rich center and a Cu-rich shell. Analysis by high-resolution TEM (HRTEM) shows that these particles consist of multiple crystalline domains, some of which cannot be matched to low chalcocite $Cu_{2-x}S$, but can be matched to either monoclinic Ga_2S_3 or wurtzite $CuGaS_2$.

Contents

1. Introduction 5

2. Theory 7

  2.1 The quantum confinement effect 7

  2.2 Semiconductor nanocrystals 9

  2.3 Synthesis of semiconductor nanocrystals 10

  2.4 Post-synthetic composition control in semiconductor nanocrystals 13

  2.5 Applications 18

3. Experimental methods 23

  3.1 Synthesis 23

  3.2 Characterization 26

4. Results and discussion 29

  4.1 Cation exchange in $Cu_{2-x}S$ bifrustums: tuning precursor reactivity 29

  4.2 Cation exchange in $Cu_{2-x}S$ bipyramids 34

  4.3 Formation of hollow nanocrystals from $Cu_{2-x}S$ bifrustum nanocrystals 37

5. Conclusion 43

6. Outlook 45

7. Acknowledgements 47

8. References 49

Appendix 55

  Appendix 1*:* Derivation of the sedimentation rate of colloidal nanocrystals 55

  Appendix 2: Derivation of the surface/volume ratio for spherical particles 56

  Appendix 3: Derivation of the critical nucleus radius 56

  Appendix 4: Miscellaneous experiments 57

  Appendix 5: Supporting and additional figures 61

1. Introduction

A metal ball dropped into a river will rapidly sink to the bottom. The same ball, shrunken until its dimensions are in the order of 1 – 100 nm, may take a few thousand years to get even half-way. Due to the extremely small size of the shrunken ball, the balance between the force of gravity and the force of drag is substantially different from the balance we observe in the macroscopic world (see Appendix 1 for a derivation). Nanoscale objects have other properties which differ substantially from those of macroscopic objects. For example: a football has a surface/volume (S/V) ratio of 3.0 m^{-1}, while this ratio is $1.7 \cdot 10^8$ m^{-1} for a spherical nanoparticle (radius 2.0 nm, see Appendix 2 for a derivation). These examples illustrate that the nanoscale world is very different from the macroscopic one, with objects not behaving as one would expect based on common-sense. Apart from making nanoparticles interesting to study, these unique properties also make them promising for a large number of applications.

Much research in particular is being done in the field of semiconductor nanocrystals (NCs). Interest in semiconductor NCs is so large because these particles may exhibit interesting opto-electronic properties. Because of their small size, the so-called *quantum confinement* effect is induced, making the size of the band gap dependent on the particle size. By tuning the band gap of semiconductor NCs, the wavelength (*e.g.,* the colour) of absorbed and emitted light can be tuned. This makes semiconductor NCs interesting for applications in photovoltaics,[1] lighting and LEDs.[2] The combination of these optoelectronic properties with small particle sizes makes semiconductor NCs especially attractive for bio labelling.[3] The ability of nanoparticles to form dispersions in liquids allows for the use of these particles in solution-processing techniques, such as inkjet printing.[4]

Much is already known about the synthesis and properties of NCs, with the production of NCs with a wide range of compositions, shapes and sizes being possible.[5] The prototypical semiconductor NC material is CdSe. NCs with this composition have been studied extensively, due to the relative ease of their synthesis and their remarkable luminescent properties.[6–9] However, these NCs are highly toxic, because they contain cadmium. Recently, NCs with a non/less-toxic composition have come into focus. Nanocrystals of ternary and quaternary semiconductors, such as $CuInS_2$, $Cu(In,Ga)S_2$ and $CuZnSnS_4$ are interesting alternatives to CdSe, because of their less-toxic composition and their attractive opto-electronic properties.[10] However, direct synthesis of these materials proves difficult, even more so when a number of different NC shapes and sizes are desired.[10] The study of other, indirect, synthesis routes is thus necessary.

A promising post-synthetic NC treatment is the cation exchange (CE) procedure. In this procedure, the original cations are extracted from the NC lattice, while new ones are incorporated. Typically, the anion sublattice is conserved during the reaction, allowing the product particles to inherit the crystal structure, shape and size of the parent particles.[11] Cation exchange thus allows for control over the composition of preformed NCs.

In some cases, the CE reaction proceeds readily and quickly, for example in the prototypical CE of Cd^{2+} for Ag^{+} in CdSe, which proceeds in under 1s.[12] However, in other cases, the execution of CE reactions is challenging, for example when the cations exhibit a low diffusivity.[13] For all CE reactions, the thermodynamics and kinetics need to be precisely controlled. If the reaction is not thermodynamically favourable, it will not happen. If the exchange rates are not balanced, the reaction may not occur, or the particles may dissolve. The use of two reactants (one to extract the native cations, one to supply the new ones), in heterovalent CE reactions (*i.e.*, CE reactions where the native and new ion have a dissimilar charge), makes balancing all these factors complicated. Recently, the use of a *single-step* cation exchange precursor was suggested to ease the execution of these CE reactions.[14] This precursor has two functions: it extracts the native cation and supplies the new one. In this way, the rate of extraction and of incorporation are coupled, allowing for greater control over the exchange rates.

In the present work, the cation exchange of Cu^{+} for Ga^{3+} in $Cu_{2-x}S$ NCs, is studied. To this end, an existing cation exchange procedure, to convert $Cu_{2-x}S$ into $CuInS_2$, is used as a starting point. The cation exchange of Cu^{+} for Ga^{3+} was chosen, because the expected product, $CuGaS_2$, is similar to $CuInS_2$ (illustrated by the synthesis of $CuIn_xGa_{1-x}S_2$ nanocrystals with x ranging from 0 to 1)[15][16], and has a direct band gap of 2.3 eV [17], making it interesting for applications in chemical sensing [18] and photocatalysis [17]. Furthermore, adaptation of the existing cation exchange procedure for use with another element may pave the way towards a more generally applicable cation exchange procedure for copper chalcogenides.

2. Theory

2.1 The quantum confinement effect

Perhaps the most interesting property of semiconductor nanocrystals (NCs) is the so-called *quantum confinement* effect: with decreasing NC size, the band gap energy increases and discrete energy levels occur at the band edges. Since the colour of emitted light (for many luminescent NCs) is dependent on the size of the band gap, the quantum confinement effect can be beautifully illustrated with luminescent NCs of different sizes (Figure 1).

The quantum confinement effect can be explained using two different approaches: a top-down approach, where NCs are regarded as very small crystals, and a bottom-up approach, where NCs are regarded as very large molecules. In the present work, we will only use the qualitative bottom-up description (a quantitative explanation can be found in Ref. [19]).

A linear combination (LCAO) of atomic orbitals (AOs) yields molecular orbitals (MOs), the number of which always equals the number of AOs. The highest occupied MO is referred to as the HOMO, the lowest unoccupied MO as the LUMO. Thus, going from systems with a small amount of atoms (*e.g.*, molecules), to systems with more atoms (*e.g.*, nanocrystals, bulk crystals), the number of MOs increases, as the number of AOs increases with the number of atoms (Figure 2)

With more AOs available, more combinations of AOs become possible. Only few combinations result in strongly bonding or anti-bonding MOs. Thus, most of the MOs reside at intermediate energy values, with only few at the edges of the MO 'cluster' (Figure 2). The MOs at the edges shift to more extreme energy values, since more AOs contribute to their total energy. The energy range of the MOs thus widens and the energy difference between the HOMO and LUMO decreases. At a certain point the number of MOs becomes so large, and the energy difference between them so small, that individual MOs can no longer be distinguished. Instead, the MO 'cluster' is treated as a continuum and referred to as a *band*. The lower, fully occupied band is referred to as the valence band (VB). The higher unoccupied band is referred to as the conduction band (CB). The energy difference between the two bands, the *band gap*, is equivalent to the energy difference between the HOMO and LUMO. If we apply the same argument, but move from a large number of AOs to a smaller number (*e.g.*, from a bulk crystal to a nanocrystal), we see an *increase* in the band gap energy and the appearance of discrete states near the band edges.[19]

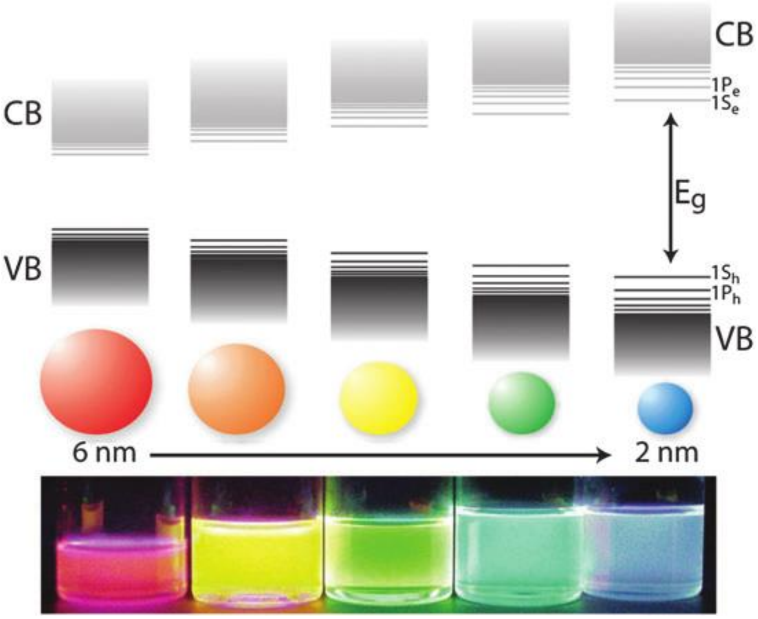

Figure 1. Top panel: Schematic showing the two main results of quantum confinement: with decreasing nanocrystal size, the band gap energy E_g increases and discrete energy levels occur near the band edge. Bottom panel: photograph of colloidal dispersions of CdSe nanocrystals with five different sizes, arranged from large to small (left to right). Reproduced from Ref. [5].

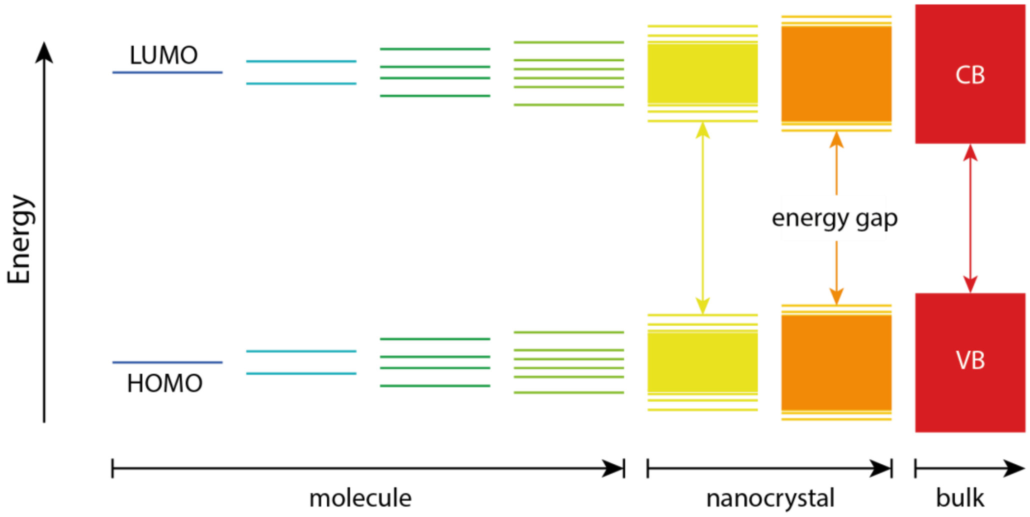

Figure 2. Energy level diagram showing the change in energy levels with increasing number of atoms. Apparent is a decrease in the energy gap and disappearance of discrete states near the band edges, with increasing number of atoms. Adapted from Ref [20].

The rainbow of colours displayed in Figure 1 is due to optical transitions in the dispersed NCs, i.e. the absorption and subsequent emission of photons. Upon the absorption of a photon, an electron is brought to a higher energy state. In NCs, this entails promotion of the electron from the VB to the CB. The resulting absence of the electron from the VB can be regarded as a quasi-particle: a *hole*, which only differs from the electron by its charge (e^+ instead of e^-) and its effective mass.[19] The electron and hole experience an attractive Coulomb interaction. The electron-hole pair can thus be described by another quasi-particle: an *exciton*.[19] The most probable distance between the electron and hole is similar to the Bohr radius (the most probable distance between an electron and a proton in a hydrogen atom). The equation for the *exciton* Bohr radius a_0 is:[21]

$$a_0 = \frac{\hbar^2 \varepsilon}{e^2}\left(\frac{1}{m_e^*} + \frac{1}{m_h^*}\right)$$

With ε the dielectric constant of the material, e the elementary charge, m_e^* the effective mass of the electron and m_h^* the effective mass of the hole. The exciton Bohr radius differs between materials, since ε, m_e^* and m_h^* are material-dependent. After absorption (neglecting other processes), the electron falls back from the CB to the VB and recombines with the hole. This process may be accompanied by the emission of a photon. The energy of this photon (and thus its colour) depends on the energy difference between the top of the VB and the bottom of the CB, i.e. the size of the band gap.

Comparison of the size of a NC to the exciton Bohr radius of its material allows for a measure of the extent of quantum confinement. When a dimension of the NC is smaller than the exciton Bohr radius, the exciton is confined in that dimension. For a spherical NC with a radius smaller than a_0, the exciton is confined in all three spatial dimensions. These NCs are then referred to as '0-D', or quantum dots (QDs). Lengthening a QD along one dimension (such that this dimension is now much larger than a_0) produces a quantum wire (1-D). Extension along another dimension a quantum well (2-D) and further elongation along the third spatial dimension a bulk crystal (3D).[19]

2.2 Semiconductor nanocrystals

Semiconductor NCs consist of an inorganic core, capped by a layer of (long chain) organic ligands, which act as stabilizers. These ligands are needed to prevent NCs from getting too close together. In this way aggregation (sintering), which is caused by the tendency of NCs to merge to lower their surface/volume (S/V) ratio, and agglomeration (clustering), which is caused by Van der Waals interactions between NCs, are prevented.[5] The ligands play an important role in the properties of NCs. For example: they determine the compatibility of NCs with solvents and influence the optical properties.[5] The ligands are also important in the synthesis of NCs, which will be discussed in more detail below.

Although NCs are often approximated as spheres, they are never truly spherical. Instead, they are facetted. The facets exposed by the NC surface depend on the crystal structure of the material. For the equilibrium shape of a NC, the size of facets depends on their relative stability.[22] A crucial factor in this regard is the coordination number (CN, *i.e.* the number of nearest neighbour atoms) of the atoms of a facet. To illustrate this principle, we use a schematic representation of a Co NC (Figure 3).[23] Atoms with lower CN have a higher chemical potential because they experience less bonding interactions (the absence of bonds is also referred to as 'dangling bonds'). To minimize its overall free energy, the NC will minimize the number of atoms in these thermodynamically unfavourable positions. The final equilibrium shape of the NC is thus a balance between the relative stabilities of the individual facets and a minimization of the overall surface area.[22] This explains why NCs are facetted: although a spherical shape best minimizes the surface area, it would require a large portion of the surface atoms to occupy positions with low CN. High-density facets account for a larger portion of the surface area than low-density ones, since the CN of their atoms is higher (Figure 3).

True NC shapes often differ from the ones predicted based on the reasoning above. One of the main reasons for this difference is that NC growth is generally kinetically controlled, meaning that the final morphology is not the thermodynamically most stable one. The organic capping ligands may play a large role in determining the final NC shape, since they may passivate the dangling bonds of surface atoms.[22]

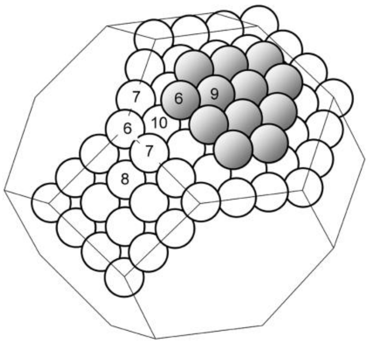

Figure 3. Schematic representation of a Co nanocrystal. Spheres denote atoms, numbers denote the coordination number (CN) of the respective atoms. Inside the crystal, the CN of atoms is largest (12). The CN of atoms in high-density facets (9, 10) is relatively close to the value inside the crystal. Atoms in lower-density facets have a lower CN (8). Atoms at edges, corners and step-edges have an even lower CN (7, 6 and 6, respectively). Reproduced from Ref. [23].

2.3 Synthesis of semiconductor nanocrystals

The synthesis of nanocrystals is well-developed, with control over NC size and shape being possible.[5] One of the main requirements in NC synthesis is that produced particles are identical (or nearly-identical) in size and shape. In other words, the NCs are required to be *monodisperse*. In practice, minor differences in shape and size between particles will always be present. However, it is possible to produce particles which have a standard deviation in their size of only a few percent.[22] To produce such monodisperse NCs, care must be taken when designing and executing the synthesis procedure. Seemingly minor differences in reaction circumstances (such as the heating rate, or the concentration of reagents) may influence the outcome of the reaction immensely. The so-called hot-injection and heating-up methods, which will be discussed later, can be used to produce monodisperse NCs.

In the formation of NCs, four stages can be discerned: (i) induction; (ii) nucleation; (iii) growth and (iv) annealing.[22] In the induction stage, the nanocrystal precursors (*i.e.*, the initial compounds that make up the reaction mixture, apart from any ligand and solvent molecules) (thermally) dissociate or react with each other to form monomers (*i.e.*, the constituents of the product NCs). Once a critical concentration of monomers is reached, NC nuclei form. An activation energy is required for the formation of these nuclei. This activation barrier follows from the thermodynamically favourable ($\Delta G < 0$) formation of the new crystal phase and the unfavourable ($\Delta G > 0$) formation of the interface of this new phase with the solution. We will use classic nucleation theory to discuss the nucleation of NCs.

The difference in free energy associated with the formation of the crystal phase (ΔG_V) scales with the volume of the nucleus. When nuclei are approximated as perfect spheres, the difference in volume free energy is thus:[22]

$$\Delta G_V = \frac{4}{3}\pi r^3 \rho \Delta\mu \tag{1}$$

With r the radius of the nucleus, ρ the density and $\Delta\mu$ the difference in chemical potential between the created volume and monomers in solution (*i.e.*, $\Delta\mu = \mu_{NC} - \mu_{monomer}$). In general, $\Delta\mu$ is negative ($\mu_{monomer} > \mu_{NC}$), thus $\Delta G_V < 0$. $\Delta\mu$ can be expressed as:[22]

$$\Delta\mu = -kTln(\frac{a}{a_0}) \tag{2}$$

With k the Boltzmann constant, T the temperature, a the monomer activity and a_0 the monomer activity when an equilibrium is reached with a macroscopic crystal in solution. High temperature and high monomer concentrations thus favour the NC formation. The difference in interfacial free energy (ΔG_S) scales with the surface area of the NC. When we again approximate the NCs as perfect spheres, we obtain:[22]

$$\Delta G_S = 4\pi r^2 \gamma \tag{3}$$

With γ the surface tension. Since γ is positive (the formation of a surface is unfavourable), $\Delta G_S > 0$. The total free energy difference (ΔG_{tot}) is the sum of ΔG_V and ΔG_S:

$$\Delta G_{tot} = \frac{4}{3}\pi r^3 \rho \Delta\mu + 4\pi r^2 \gamma \tag{4}$$

Using Equation 4, an equation for the critical nucleus radius (r_c) can be derived (Appendix 3), yielding:

$$r_c = -\frac{2\gamma}{\rho\Delta\mu} \tag{5}$$

The critical nucleus radius coincides with the position of the activation barrier for nucleus formation (Figure 4). Note that $\Delta\mu$ is negative, the minus sign in Equation 5 is thus required to ensure that r_c is positive. Entering Equation 5 into Equation 4 yields an expression for the height of the activation barrier (ΔG_c):

$$\Delta G_c = \frac{16\pi\gamma^3}{3\rho^2\Delta\mu^2} \tag{6}$$

The formation of nuclei thus involves an activation barrier, which must be overcome for nucleation to occur (Figure 4).

To obtain monodisperse NCs, a separation of the nucleation and growth stages is required. If these stages are not temporally separated, new NCs form while others are already growing, resulting in a wide size distribution. Since the position (r_c) and height (ΔG_c) of the activation barrier both depend on $\Delta\mu$, the activation barrier can be altered by controlling $\Delta\mu$. By momentarily increasing $\mu_{monomer}$ (*i.e.*, making the value of $\Delta\mu$ more negative), r_c and ΔG_c will momentarily decrease, allowing nucleation for only a short period of time.[22]

In the hot-injection method, this is done by the injection of a cold reactant into a hot mixture of another reactant. At the moment of injection, both the temperature and monomer concentration are high (thus $\mu_{monomer}$ and $|\Delta\mu|$ are large), resulting in a small r_c and ΔG_c, allowing nucleation. Upon the formation of nuclei, monomers are incorporated, thus their concentration drops dramatically. This is accompanied by a drop in temperature (due to the low temperature of the injected solution). $\Delta\mu$ becomes less negative, thus resulting in larger r_c and ΔG_c, preventing further nucleation.[22]

In the heating-up method, r_c and ΔG_c are momentarily lowered by increasing the temperature of a mixture containing the required reactants. The reactants rapidly decompose and form monomers, momentarily raising the monomer concentration (thus lowering r_c and ΔG_c, allowing nucleation). The formation of nuclei is accompanied by a drop in monomer concentration and an increase in r_c and ΔG_c, preventing further nucleation.[22]

If the rate of nucleation is high, many small nuclei will form and the subsequent monomer activity will be relatively low. If the rate of nucleation is low, the number of nuclei will be smaller, the nuclei will be larger and the subsequent monomer activity will be relatively large. The rate of nucleation can be adjusted using (organic) ligands, since these bind to monomers and nuclei. The precursor concentration and reaction temperature also influence the rate of nucleation.[22]

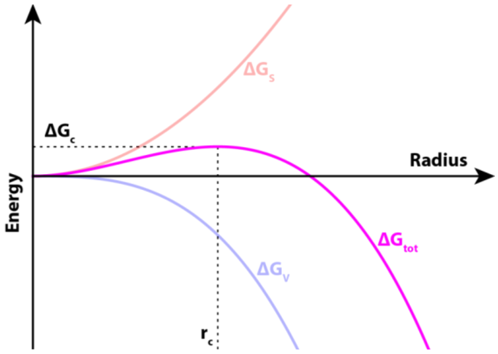

Figure 4. Graph depicting the total free energy of the formation of nanocrystal nuclei, as a function of nucleus radius. The maximum of the graph coincides with the critical free energy of nucleation. The position of the maximum coincides with the critical nucleus radius.

We will discuss two ways of NC growth: growth by addition of monomers and growth by coalescence of individual NCs. In the case of growth by addition of monomers, monomers need to diffuse to the surface of the NC, and then need to be incorporated into the crystal. Diffusion of monomers to the NC surface is driven by a gradient in the monomer concentration in the solution.[22] At higher monomer concentrations, the diffusion sphere is small and may be similar in size to the NC. This results in different parts of the NC experiencing different effective monomer concentrations. Since the growth rate depends on the monomer concentration, this results in anisotropic growth.[22] Anisotropic growth can also be caused by a difference in reactivity of the different surface facets: the growth rate along a facet increases exponentially with the facet free energy. Ligands may influence the growth rates along the facets they bind to. This influence is twofold: they both thermodynamically stabilize the facet atoms (by increasing their coordination number) and kinetically restrict the incorporation of new monomers (because the ligand first needs to be displaced before a new monomer can be added). Because ligands may show a preference for certain facets over others, the right choice of ligands allows for control over the NC shape.[5,26,27]

NCs may also grow by coalescence. First, individual NCs form by addition of monomers. Then, these NCs coalesce, forming larger NCs. A special case of growth by coalescence is oriented attachment: aggregates of coalesced NCs fuse and undergo reconstruction, resulting in a single monocrystalline (anisotropic) NC. The formation of aggregates and orientation of NCs is thought to be due to dipolar interactions between NCs.[22]

2.4 Post-synthetic composition control in semiconductor nanocrystals

Limitations of direct synthesis approach

There are a number of ways in which the composition of NCs can be controlled. The most obvious is the choice of precursors used in the direct synthesis of NCs. NCs with a wide range of compositions can already be prepared via direct synthesis.[5] Binary NCs can readily be produced by thermolysis of two different precursors (a cation and an anion precursor). Although more difficult, the same approach can be taken to produce ternary NCs, and even quaternary ones.[10] The need to balance the reactivities of the different precursors, to prevent undesired formation of hetero-nanocrystals (HNCs) or nucleation of two different types of NCs, makes this approach challenging for the synthesis of ternary and quaternary NCs.[10] Often, only few morphologies (if not only one) can be prepared in this manner.[10] Even for binary NCs, the synthesis may yield NCs with the required composition, but it may not be possible to obtain the desired crystal structure (or morphology). Therefore, post-synthesis procedures are interesting, since they allow for modification of preformed NCs.

Cation exchange

Cation exchange (CE) is a versatile post-synthesis procedure that can be used to produce NCs with a combination of shape, composition and crystal structure not attainable by direct synthesis.[11] This is due to the fact that product NCs inherit their size, shape and crystal structure from their parent NCs. As implied by the name, CE entails the exchange of the native cation species in a crystal for different cations. To this end, the original cations are extracted from the crystal lattice, while the new ones are incorporated. The stability of the anionic sublattice, due to the large size of the anions, allows for the exchange of cations, while the anionic sublattice remains unchanged. The shape and crystal structure may thus be preserved.[11] In its most simple form, CE is performed by combining the parent NCs with a solution of the new cation. An example of such an approach is the conversion of CdSe into Ag_2Se, by addition of Ag^+, dissolved in methanol, to a dispersion of CdSe nanocrystals.[12]

Due to a number of nanoscale effects, cation exchange reactions may readily occur in nanocrystals, while they do not occur (or proceed very slowly) in macroscopic crystals. In general, nanocrystals have a higher surface free energy than macroscopic crystals, due to their high surface/volume ratio.[22] This lowers the activation energy for cation exchange at the crystal surface. Furthermore, diffusion rates in NCs have been observed to be much faster than in bulk.[26] These factors greatly benefit cation exchange reactions in nanocrystals and make them relatively easy to perform, compared to cation exchange reactions in macroscopic crystals.

Thermodynamics of cation exchange

While thermodynamics dictates the position of the equilibrium in chemical reactions (and thus whether or not the reaction will proceed), it also influences the activation barriers and thus the kinetics involved. On the other hand, while a reaction may be thermodynamically favourable, kinetic factors may prevent the reaction from occurring, for example when an activation barrier is too high to be overcome at the reaction temperature. Furthermore, species cannot react with one another if they are not close together. Diffusion can thus also be a limiting factor. This interplay between thermodynamics and kinetics makes it difficult to separate the two. However, separately discussing the two may be informative, provided that heir intertwined nature is kept in mind: the combination of both determines the actual reaction outcome.

The driving force for cation exchange reactions are the relative stabilities of the reactant and product phases, and the relative stabilities of the (solvated) cations.[11] Given a generalized cation exchange reaction:

$$AS(s) + B^{2+}(sol) \rightarrow BS(s) + A^{2+}(sol) \tag{7}$$

The free energy of the reaction can be described as (assuming constant temperature and pressure):

$$\Delta G_r = \Delta\mu_{crystal} + \Delta\mu_{cations} = \mu_{BS} - \mu_{AS} + \mu_{A2+} - \mu_{B2+} \tag{8}$$

With $\Delta\mu_{crystal}$ the difference in chemical potential between the product phase and the initial phase, $\Delta\mu_{cations}$ the difference in chemical potential between the product cations and the reactant cations, μ_{BS} and μ_{AS} the chemical potentials of the product and reactant crystal phases, respectively, and μ_{A2+} and μ_{B2+} the chemical potentials of the product and reactant (solvated) cations, respectively. Requirement for spontaneous reaction is $\Delta G_r < 0$, which requires that the sum of μ_{AS} and μ_{B2+} is larger than the sum of μ_{BS} and μ_{A2+}.

The chemical potential of the crystal phases depends on a number of factors, such as crystal structure, NC morphology and the ligands that cap the NC.[11] This makes it difficult, if not impossible, to adjust μ_{AS} or μ_{BS} selectively for a given NC. However, the cationic contributions are easier to manipulate. A high B^{2+} concentration will raise μ_{B2+} and bring the system in a non-equilibrium state. To re-establish equilibrium, the system must convert reactants into products, thus ‘forcing’ the formation of the product. This is the reason why an excess amount of the reactant cation is often used in CE reactions (although it is not required for all CE reactions).[11] The downside of a higher concentration is an increase in the reaction rate, which may make the reaction difficult to control, possibly yielding undesired products. It is also possible to increase the thermodynamic driving force by lowering μ_{A2+}. This can be done by selectively ligating the product cations. An example is the use of a soft Lewis base to preferentially ligate a soft product cation and not the harder reactant cation. Tertiary phosphines ($\eta \approx 6$ eV)[11] are commonly used as selective ligands for soft cations, such as Cu^+ ($\eta = 6.28$ eV)[27] and Ag^+ ($\eta = 6.96$ eV)[27], in CE reactions for harder cations, such as Zn^{2+} ($\eta = 10.88$ eV)[27] and Cd^{2+} ($\eta = 10.29$ eV)[27].[12,27,28]

Kinetics of cation exchange

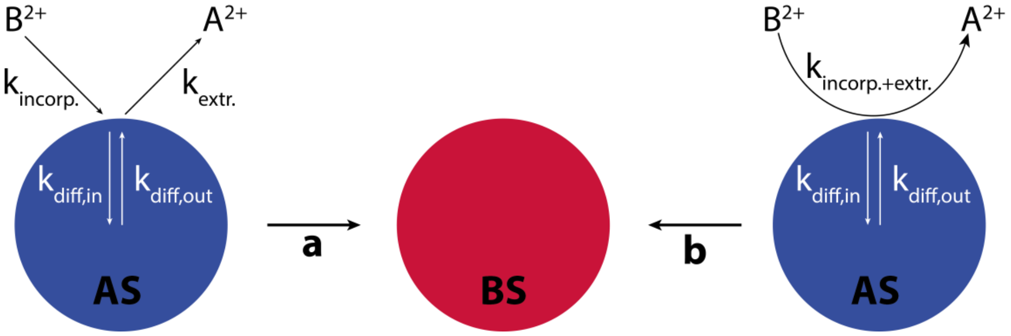

Figure 5. Scheme depicting two generalized cation exchange reactions: (a) using two reaction precursors; (b) using a single-step reaction precursor. $k_{incorp.}$ and $k_{extr.}$ denote the B^{2+} incorporation and A^{2+} extraction rate at the nanocrystal surface, respectively. $k_{diff,in}$ and $k_{diff,out}$ denote the inward diffusion rate of B^{2+} and the outward diffusion rate of A^{2+}, respectively. $k_{incorp.+extr.}$ denotes the coupled incorporation rate of B^{2+} and extraction rate of A^{2+} at the nanocrystal surface.

CE reactions are usually kinetically controlled.[11] Kinetic factors are thus very important in determining the outcome of the reaction. For the exchange to proceed, four steps need to occur: (i) extraction of native cations from the NC surface; (ii) incorporation of new cations at the NC surface; (iii) diffusion of the new cations into the NC; (iv) diffusion of native cations from the inside of the NC to the NC surface (Figure 5a). If any of these steps does not occur, the CE stops. The exchange at the surface (steps (i) and (ii)) favours the diffusion of cations (steps (iii) and (iv)), since it induces a concentration gradient in the NC.[11]

It is important to balance the rate of extraction ($k_{extr.}$) and the rate of incorporation ($k_{incorp.}$). Otherwise the CE may not occur at all, the NC may dissolve, or voids may form.[14,30] Often, in heterovalent CE reactions, two different reactants are used for step (i) and (ii): one to supply the reactant cation and one to extract the native cation.[12,28,29] While this approach was used successfully in the past, it requires a tuning of the reaction parameters (*e.g.*, temperature, concentration of parent NCs, of cation extracting reactant and of cation supplying reactant, reactivity of cation extracting reactant and of cation supplying reactant), which may make CE reactions difficult to control. Recently, a *single-step* precursor was employed to mitigate this issue in heterovalent CE reactions. This precursor acts both as new cation supplier and native cation extractor, thus coupling the rates of extraction and of incorporation (Figure 5b).[14]

Apart from the exchange at the surface, diffusion of cations inside the NC is also an important kinetic factor. Before the system reaches its final composition, it first has to go through an intermediate phase. The region in which the crystal has an intermediate composition is referred to as the reaction zone.[11] The reaction zone forms at the NC surface and moves inwards due to the diffusion of cations. Depending on the material, NC size, and reaction conditions, the reaction zone may be comparable in size to the NC, or it may be smaller.

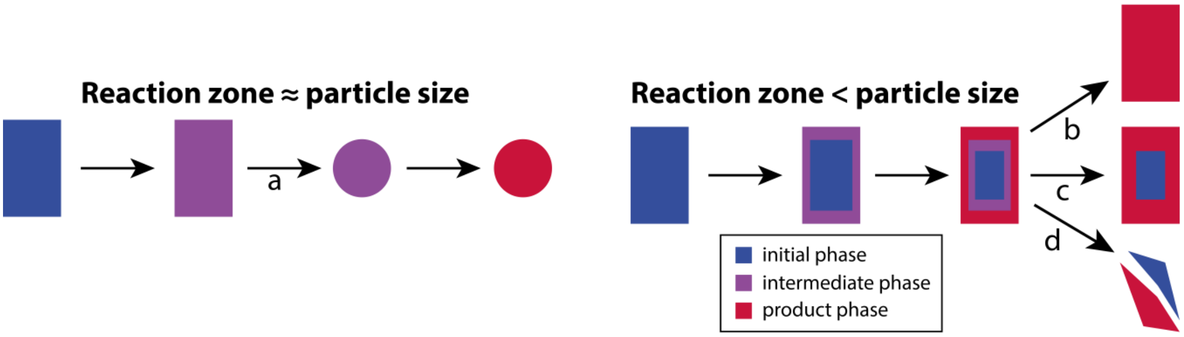

Figure 6. Schematic depicting the results of cation exchange reactions. Left scheme depicts the progress of the reaction when the reaction zone is similar in size to the NC: (a) the whole particle is temporarily in an unfavourable state and changes morphology to lower its free energy. Right scheme depicts the progress of the reaction when the reaction zone is smaller than the particle size: (b) the lattice mismatch is relatively small, the nanocrystal can accommodate the strain and the exchange proceeds to completion; (c) the lattice mismatch is sufficiently large to prevent complete exchange, or solid-state diffusion is slow, resulting in a heterostructure; (d) the lattice mismatch is too large, the particle fragments, or voids form. Figure partially adapted from Ref. [12].

In the former case, the whole NC may momentarily be in a thermodynamically unfavourable state. Instead of the CE proceeding, the NC may at this point change its morphology and crystal structure to lower its free energy (Figure 6a).[12] This is usually undesirable, since the shape, size and crystal structure of the parent NC are then lost.

When the NC is large compared to the size of the reaction zone, only a portion of the crystal is affected at a time, resulting in a local distortion or strain due to a lattice mismatch between the reactant phase and the product phase. If the lattice mismatch is small enough, the system will be able to accommodate the distortion or strain and the exchange will proceed (Figure 6b).[11] If the mismatch is too large, the exchange may stop (resulting in heterostructures, Figure 6c)[31], the NCs may fragment or voids may form (Figure 6d).[32] Heterostructures may also form due to slow diffusion, even in cases where the lattice mismatch is small (Figure 6c).

The diffusivity of the cations may also be the limiting process in the CE. This was the case in the exchange of Zn^{2+} for Cd^{2+} in ZnSe NCs.[26] This exchange was characterized by an initial fast cation exchange at the NC surface, followed by slow diffusion of Zn^{2+} and Cd^{2+} within the crystal. Because the rate of diffusion is temperature dependent in this case, the authors were able to prepare HNCs by CE at a low temperature and homogenous $Zn_xCd_{1-x}Se$ NCs by reacting at a higher temperature.[26] There are thus a number of regimes where CE proceeds only partially, ranging from a partial homogeneous exchange, to the formation of HNCs. This shows that CE is not simply limited to the conversion of one material into another: it also makes intermediate compositions and novel heterostructures accessible.

$Cu_{2-x}S$ nanocrystals as templates for ternary and quaternary nanocrystals

$Cu_{2-x}S$ nanocrystals are an interesting class of nanocrystals. They can be produced in a variety of shapes, including nearly spherical particles, bifrustums, bipyramids, nanoplatelets and nanosheets.[10] The '*x*' in $Cu_{2-x}S$ denotes intrinsic Cu^+ vacancies, the charge of which is compensated for by free holes. Because of these holes, $Cu_{2-x}S$ nanocrystals may show a strong, broad absorption band, which is due to the plasmon resonance of these free charge carriers.[33] $Cu_{2-x}S$ nanocrystals are interesting for the present study, because they can be used as templates for the production of ternary and quaternary nanocrystals with interesting opto-electric properties. Among these ternary and quaternary nanocrystals are $CuInS_2$, $CuIn_xGa_{1-x}S_2$ and Cu_2ZnSnS_4, which are useful for applications in lighting, photocatalysis and photovoltaics.[10] The possibility of synthesizing $Cu_{2-x}S$ NCs with different crystal structures allows for even more flexibility. By using $Cu_{2-x}S$ NCs with a zinc-blende like crystal structure as cation exchange parent NCs, ternary and quaternary NCs can be obtained which have a crystal structure similar to zinc-blende (chalcopyrite for tertiary ones, kesterite and stannite for quaternary ones)[10], since the crystal structure after CE is inherited from the parent particles.[10,11] Likewise, quaternary and ternary analogues with the wurtzite crystal structure can be obtained when low-chalcocite $Cu_{2-x}S$ NCs are used as parent particles.

$Cu_{2-x}S$ NCs are well-suited as template materials, since they undergo CE reactions relatively easily. This is partially due to the small size and high diffusivity of the Cu^+ cation in $Cu_{2-x}S$. The availability of relatively soft ligands which preferentially bind to the equally soft Cu^+ ($\eta \approx 6$ eV for both Cu^+ and tertiary phosphines)[11,27] further eases the execution of CE reactions in these NCs.[10]

2.5 Applications

As briefly mentioned in the introduction, semiconductor NCs have numerous applications. A number of these possible applications will be discussed below.

Solar cells

At the time of writing, silicon-based solar cells are produced on an industrial scale and the sight of these solar cells on the rooftops of buildings is normal. Although the production of these solar cells is economically viable and although they are widely adopted by consumers, they still have a number of disadvantages. The maximum efficiency is relatively low (~15%), production and installation are costly, and the cells need to be thick.[1] To some extent this is because silicon has an indirect band gap. Any absorption of light is thus necessarily phonon-assisted, resulting in a low absorption coefficient, thus requiring a thick solar cell.[34]

Semiconductor NC-based solar cells are an attractive alternative to silicon-based ones. Since the absorption spectrum of NCs is tuneable by tuning their size, a higher portion of the solar spectrum may be absorbed. When NCs with a direct band gap are used, their absorption coefficient will be significantly larger than silicon, allowing for a thinner solar cell layer, reducing the amount of materials needed and decreasing the weight of the cell.[1] Because colloidal NCs are solution-processable, the production can make use of cheap techniques, such as inkjet printing.[4]

The generation of electricity in a semiconductor NC-based solar cell is based on charge separation. As a photon is absorbed by a NC, it excites an electron to the conduction band (CB), leaving a hole in the valence band (VB). In a solar cell, the electron and hole are then separated, generating an electric current (Figure 1a). To facilitate the charge separation, a layer containing the NCs is placed between an electron transport layer and a hole transport layer (Figure 1a).[1] The band edges of the hole transport layer, the NCs and the electron transport layer should be chosen carefully, so the electrons move from the NCs to the electron transport layer and the holes to the hole transport layer (Figure 1b). In this manner, the photo-generated electron and hole are separated, resulting in an electric current.

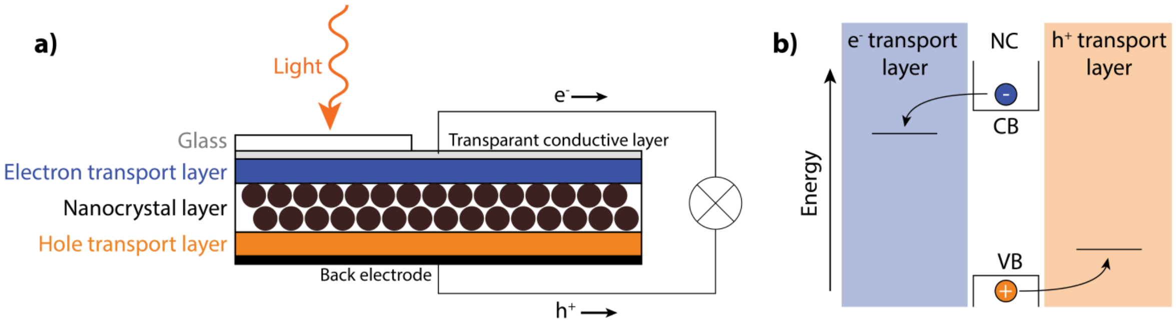

Figure 7. (a) Schematic representation of the general layout of a nanocrystal solar cell, showing the different layers that make up the solar cell; (b) an energy level diagram showing the principle behind separation of the electron-hole pair: energy levels of the electron transport layer and the hole transport layer are chosen such that the electron and hole each relax into the electron transport layer and hole transport layer, respectively. They are thus spatially separated. Images designed based on descriptions in [1] and [35]**.**

Light emitting diodes

Semiconductor nanocrystals are promising for applications in light emitting diodes (LEDs). Large advantages of NCs for this type of application are the fact that they are solution-processable (simplifying production and lowering production costs), have a narrow emission wavelength (typical full-width at half-maximum values for emission peaks are ~30nm), and are potentially more stable than LEDs based on organic luminophores (OLEDs).[2] The production of NC LEDs is well developed, with devices being adapted in consumer electronics (these LEDs are then often referred to as 'QD LEDs').[36]

The operation of a NC LED can be compared to the reverse operation of a NC solar cell: instead of light being absorbed, light is emitted and instead of a separation of charges from the NCs, charges are injected into the NCs. The applied electric potential allows for promotion of electrons from the electron transport layer to the CB and of holes from the hole transport layer to the VB. The injected charges recombine in the NC, emitting a photon.[2]

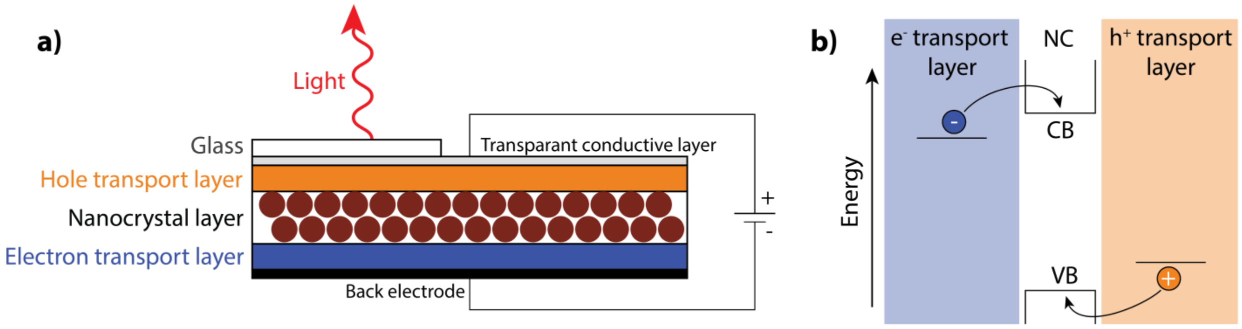
a)
Light
Glass
Transparant conductive layer
Hole transport layer
Nanocrystal layer
Electron transport layer
Back electrode
+
-
b)
e⁻ transport layer
NC
h⁺ transport layer
CB
VB
Energy
-
+

Figure 8. (a) Schematic representation of the general layout of a nanocrystal light emitting diode, showing the different layers that make up such a diode; (b) an energy level diagram showing the principle of charge injection: electrons are transferred from the electron transfer layer into the conduction band of the nanocrystals, while holes are transferred from the hole transport layer into the valence band of the nanocrystals. Images designed based on descriptions in [2].

Luminescent solar concentrators

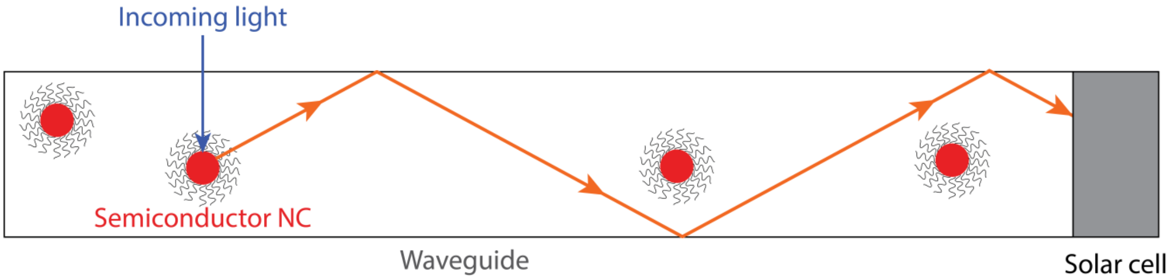

Figure 9. Schematic representation of a luminescent solar concentrator. Incoming light is absorbed by semiconductor nanocrystals, emitted at a longer wavelength and guided to a solar cell via total internal reflection, where the light is absorbed. Image based on descriptions in [37]**.**

While solar cells are a promising way of generating renewable energy, they possess a number of downsides. Solar cells are relatively expensive, heavy and are only available in a limited number of colours (mostly dark blue and black).[37] Furthermore, solar cells perform best under direct sunlight. Due to these downsides, solar cells cannot be applied to the majority of outdoor surfaces: most surfaces only experience diffuse sunlight. Solar cells applied to these surfaces thus generate little electricity. Surfaces which should be transparent, such as windows, are not suitable either. Solar cells placed on these surfaces would absorb all light before it could pass through, negating the purpose of these surfaces.

Luminescent solar concentrators (LSCs) may proof a good addition to solar cells, because they do not exhibit the same downsides. LSCs concentrate a portion of the solar light onto solar cells, by absorbing a portion of the solar spectrum and re-emitting it at a longer wavelength (Figure 9). LSCs are relatively cheap, compared to solar cells, and can be placed on surfaces where solar cells are not suitable. For example, LSCs, which only absorb in the ultra-violet region of the spectrum, can be integrated in windows. Furthermore, LSCs perform well under both direct and diffuse illumination, allowing their application to surfaces which do not experience direct sunlight.[37]

LSCs work by the absorption of incoming light by a luminophore, followed by emission at a longer wavelength. The emitted light is guided to a solar cell at the edge of the LSC, through total internal reflection within the waveguide (Figure 9). For optimal operation of these devices, it is important to prevent energy loss processes. Two key processes are reabsorption of emitted light and emission of light at the wrong angle, preventing total internal reflection.

There are a number of options for the luminophore in LSCs. Organic dyes may appear attractive, since these can have a high luminescent quantum yield (>95%)[37]. However, the energy difference between the maximum of absorption and maximum of emission (the so-called ‘global Stokes-shift’) is generally small, with considerable overlap between absorption and emission. The resulting reabsorption of emitted light (also referred to as self-absorption) lowers the overall efficiency of the device, since energy is lost via non-radiative relaxation pathways, or photons may be re-emitted at angles which allow the light to escape the LSC. Use of luminophores with a relatively large Stokes-shift is thus preferable.[37]

Semiconductor NCs may be well-suited as luminophores, because of their size-tuneable absorption and emission spectrum. Furthermore, some NCs exhibit a large Stokes-shift. Tuning of the absorption spectrum allows the LSC to absorb only a portion of the solar spectrum, while remaining transparent to the rest of the spectrum. In this way, windows can be coated with LSCs which only absorb ultra-violet light, allowing the windows to remain transparent.

Bio imaging

For treatment of certain diseases, such as cancer, the detection and localization of the affected area within the body can help greatly with treatment of the disease. Common imaging techniques such as magnetic resonance imaging (MRI) and computed tomography (CT) offer imaging of tissue without penetration-depth limitations. However, the spatial resolution obtainable with these techniques is limited.[3] Fluorescence microscopy may afford a higher spatial resolution. To this end, luminescent NCs can be used. Because of their small size, the obtainable spatial resolution is only limited by the diffraction limit of light (which ranges from 200 to 600 nm for visible and near-infrared light), thus offering a much higher spatial resolution.[3] The disadvantage of fluorescence microscopy is that the penetration depth is limited. The relatively broad excitation spectrum of semiconductor NCs allows for simultaneous excitation of differently sized NCs with one excitation source, allowing for simultaneous imaging with differently coloured luminophores.[38] Furthermore, the surface of NCs can be functionalized, to bind specifically to the cells/tissue which are of interest in the analysis.[39]

There are a number of factors of importance to NCs which are to be used for bio-imaging. NCs should be bio-compatible: they should not degrade under atmospheric conditions and should disperse well in water. Furthermore, the emitted light should not be absorbed by tissue. To prevent degradation of the particles, an air-stable material should be chosen. If this is not directly possible, an air-stable shell may be grown over the NCs.[38,39] Dispersion in water is possible by coating the NCs with hydrophilic ligands.[3,38,39] NCs which adhere to the mentioned requirements have already been used in *in vivo* imaging of tumours, and show great promise for tumour identification (Figure 10).[3]

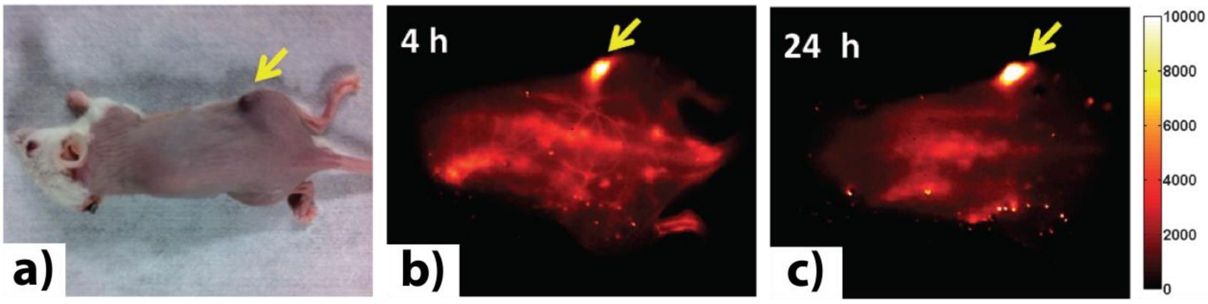

Figure 10. (a) Optical photograph of mouse injected with luminescent quantum dots, 24h after injection; fluorescence images (wavelength ~1200nm) of the same mouse (b) 4h and (c) 24h after injection of the quantum dots. The arrow indicates the location of the tumor. Images adapted from Ref. [3].

3. Experimental methods

3.1 Synthesis

Materials

Copper(II) sulfate pentahydrate ($CuSO_4 \cdot 5H_2O$, 99.995%), oleic acid (OA, tech., 90%), 1-dodecanethiol (DDT, >=98%), copper(I) chloride (CuCl, 97%), tin(IV) bromide ($SnBr_4$, 99%), oleylamine (OLAM, tech., 70%), trioctylphosphine oxide (TOPO, tech., 90%), copper(I) acetate (CuOAc, 97%), 1-octadecene (ODE, tech., 90%), diphenyl ether (DPE, 99%), gallium(III) chloride ($GaCl_3$, anhydrous, beads), trioctyl phosphine (TOP, 90%), diphenyl phosphine (DPP, 98%), triphenyl phosphite (TPP, 97%), anhydrous methanol, anhydrous butanol and anhydrous toluene were purchased from Sigma-Aldrich and used as supplied, except for OA, OLAM, ODE and TOPO, which were degassed prior to use.

Synthesis of $Cu_{2-x}S$ bifrustum nanocrystals

$Cu_{2-x}S$ bifrustum nanocrystals were prepared according to the method described in [33]. 0.203 g $CuSO_4 \cdot 5H_2O$, 6 mL OA and 7.5 mL DDT were brought into a three-necked round bottom flask, connected to a Schlenk-line. Under constant stirring and nitrogen atmosphere, the mixture was heated to 200°C (at a rate of circa 30°C/min). After reaction for 2 h at 200°C, the mixture was allowed to cool down to approximately 110°C, when it was quenched by injection of 5 mL toluene. The product was precipitated by addition of methanol and butanol as non-solvent and isolated by centrifugation at 2500 revolutions per minute (rpm), for 10 minutes. The supernatant was removed and the residue was redispersed in toluene. The mass of product was estimated by weighing the empty sample vials prior to sample retrieval and after removal of the supernatant. The amount of toluene used to redisperse the particles was chosen such, that a particle concentration of approximately 20 g/L was obtained.

Synthesis of $Cu_{2-x}S$ bipyramid nanocrystals

$Cu_{2-x}S$ bipyramid nanocrystals were prepared according to the method described in [40]. 0.165 g CuCl, 0.316 g $SnBr_4$, 13.2 mL DDT and 3.3 mL OLAM were brought into a three-necked round bottom flask, connected to a Schlenk line. Under constant stirring and nitrogen atmosphere, the mixture was heated to 225°C. The mixture was then allowed to cool down to approximately 110°C, when it was quenched by injection of 5 mL toluene. The product was precipitated by addition of methanol and butanol as non-solvent and isolated by centrifugation at 2500 rpm, for 10 minutes. The supernatant was removed and the residue was redispersed in toluene. The mass of product was estimated by weighing the empty sample vials prior to sample retrieval and after removal of the supernatant. The amount of toluene used to redisperse the particles was chosen such, that a particle concentration of approximately 20 g/L was obtained.

Synthesis of small, nearly-spherical $Cu_{2-x}S$ nanocrystals

Small, nearly spherical $Cu_{2-x}S$ nanocrystals were prepared according to the method described in [33]. 0.108 g CuOAc and 50 mL ODE were brought into a three-necked round bottom flask, connected to a Schlenk line. Under vacuum, the mixture was degassed by heating at 100°C for 30 minutes. Then, under nitrogen atmosphere, the mixture was heated to 160°C. At this temperature, 2 mL DDT was swiftly injected. The temperature was then raised to 180°C, and maintained for 195 min. The mixture was then allowed to cool down to approximately 110°C, when it was quenched by injection of 5 mL toluene. By-products and left-over reactants were precipitated by centrifugation at 2500 rpm, for 10 min. The supernatant, containing the product, was decanted. This procedure was performed three times. Then, the product was precipitated by addition of methanol and butanol as non-solvent and isolated by centrifugation at 2500 rpm, for 10 min. The supernatant was removed and the residue was redispersed in toluene. The mass of product was estimated by weighing the empty sample vials prior to sample retrieval and after removal of the supernatant. The amount of toluene used to redisperse the particles was chosen such, that a particle concentration of approximately 20 g/L was obtained.

Preparation of cation exchange precursors

Ga/In-precursors were prepared in a way similar to a previously reported method:[14]

$InCl_3$-TOP was prepared by addition of 1.250 mL (2.8 mmol) TOP to an equimolar amount (0.620 g) of $InCl_3$, then heating to 50°C under constant stirring. The resulting turbid, white, viscous liquid was diluted by addition of 1.250 mL toluene.

$GaCl_3$-TOP was prepared by addition of 0.500 mL (1.12 mmol) TOP to an equimolar amount (0.197 g) of $GaCl_3$, then heating to 50°C under constant stirring, yielding a transparent, orange, viscous liquid.

$GaCl_3$-DPP was prepared by addition of 0.815 mL (4.683 mmol) DPP to an equimolar amount (0.8246 g) of $GaCl_3$, heated to 50°C under constant stirring. After a few minutes, an opaque, white, viscous liquid formed. After a number of hours, the liquid changed into an opaque, white, crystalline solid, which was dissolved in 10 mL toluene at 100°C.

$GaCl_3$-TPP was prepared by addition of 1.125 mL (4.281 mmol) TPP to an equimolar amount (0.7538 g) of $GaCl_3$, heated to 50°C under constant stirring. After a few minutes, an opaque, white, crystalline solid formed, which was dissolved in 10 mL toluene at 100°C.

$GaCl_3$ cation exchange precursor was prepared by making a 1 mol/L (176.08 g/L) solution of $GaCl_3$ in toluene, resulting in a transparent, bright green liquid. It was found that the solution degraded over time, even when stored under inert atmosphere. Degradation was indicated by a change of colour from bright green to dark red. Therefore, in all reactions with $GaCl_3$ as precursor, a fresh batch of precursor was used.

Cation exchange in $Cu_{2-x}S$ bifrustum nanocrystals

The cation exchange reactions were performed in a way similar to that reported in [14]. The equivalent of 0.2 mmol cation exchange precursor (0.200 mL $InCl_3$-TOP, 0.100 mL $GaSCl_3$-TOP, 0.425 mL $GaCl_3$-DPP, 0.465 mL $GaCl_3$-TPP, 0.200 mL $GaCl_3$ solution) was placed in a vial. Toluene was added to make the total reaction volume after addition of the parent dispersion 2.700 mL (added volume: with $InCl_3$-TOP: 2.000 mL, with $GaCl_3$-TOP: 2.100 mL, with $GaCl_3$-DPP: 1.775 mL, with $GaCl_3$-TPP: 1.735 mL, with $GaCl_3$: 2.000 mL). The mixture of toluene and cation exchange precursor was heated to the reaction temperature (with $InCl_3$-TOP, $GaCl_3$-TOP, $GaCl_3$-DPP, $GaCl_3$-TPP: 100°C; with $GaCl_3$: 30°C) under constant stirring at 400 rpm. Once the desired temperature was reached, 0.500 mL parent NC dispersion (equivalent to approximately 10 mg parent particles) was swiftly injected. The reaction was stopped by removing the vial from the heater and quenched by the addition of methanol and butanol as anti-solvents. All samples were washed at least twice prior to analysis, by addition of methanol and butanol as non-solvent, centrifugation and removal of the supernatant. Finally, the particles were redispersed in toluene.

Cation exchange in $Cu_{2-x}S$ bipyramid nanocrystals

$Cu_{2-x}S$ bipyramid nanocrystals were cation exchanged in a procedure similar to the bifrustum ones. Changes from the method described above are: the use DPE instead of toluene, and mixing of the particles, solvent and cation exchange precursor, prior to heating to the reaction temperature of 200°C. Reactions were allowed to continue overnight.

3.2 Characterization

Unless noted otherwise, characterization was performed at the Debye Institute for Nanomaterials Science at Utrecht University.

Optical spectroscopy

Ultra-violet, visible, near-infrared absorbance spectroscopy

Ultra-violet, visible, near-infrared (UV-vis-NIR) absorbance spectra were measured using a Perkin Elmer Lambda 16 UV-vis-NIR spectrometer. Samples were prepared by placing a diluted dispersion of nanocrystals (NCs) in toluene in a quartz cuvet with 10 mm path length.

Photo-luminescence and excitation spectroscopy

Photoluminescence and excitation spectra were measured using a Edinburgh instruments FL920 spectrofluorimeter. The apparatus was equipped with a 450 W xenon lamp as excitation source and double grating monochromators. Emitted light was detected using a Hamamatsu R5509-72 photomultiplier tube, cooled to -80°C with liquid nitrogen. Samples were prepared in a similar way to samples prepared for UV-vis-NIR measurements.

X-ray diffraction

X-ray diffraction patterns were measured using a Bruker D2 Phaser, equipped with a Cu Kα X-ray source ($\lambda = 1.54184$ Å). Samples were prepared by drop-casting NCs dispersed in chloroform onto a Si wafer, and evaporating the chloroform.

Electron microscopy

Transmission electron microscopy

Transmission electron micrographs (TEM) were recorded on Philips Tecnai 10, Tecnai 12 and Tecnai 20 electron microscopes. TEM samples were prepared by drop-casting a dispersion of particles in toluene onto a copper or aluminium TEM-grid, pre-coated with a carbon-coated polymer layer.

Energy-dispersive x-ray spectroscopy

Energy-dispersive x-ray spectroscopy (EDX) measurements were performed on a Philips Tecnai 20 electron microscope. Sample preparation was similar to the preparation of TEM samples. In all cases aluminium TEM-grids were used to prevent the signal of the TEM-grids from interfering with the measurements. Measurements were performed on areas with > 500 nanoparticles. Estimated error in EDX measurements ≈ 5%. Discussed elemental compositions are normalized to the expected sulphur contents.

Elemental mapping

Elemental mapping was performed on a Talos F200X electron microscope with a 200 kV XFEX electron beam. Detection was done using four symmetrically placed SuperX-EDX detectors. Measurements were performed in high-angle annular dark-field scanning transmission electron microscopy (HAADF-STEM) mode, with a current of 700 pA. Detection in this mode was done using a Fischione Instruments HAADF detector. Obtained data were quantified and plotted using the Bruker Esprit software package.

High-resolution transmission electron microscopy

High-resolution TEM (HRTEM) micrographs were recorded at the Electron Microscopy for Materials Science (EMAT) research group at the University of Antwerp, by Mert Kurttepeli. The electron microscope used was a FEI Tecnai Osiris, operated at 200 kV. Fast fourier-transform (FFT) of micrographs of selected nanocrystals and indexation of these FFT patterns was done using the CrysTBox diffractGUI software (version 2.19).[41] The latter analyses were performed at the Debye Institute.

Tomography

HAADF-STEM tomography was performed at the EMAT research group as well, by Mert Kurttepeli. Tilt series for electron tomography were acquired from TEM samples with a FEI Tecnai Osiris operated at 200 kV in combination with an advanced tomography holder from Fischione Instruments and the FEI XPlore3D acquisition software. Tilt series consisting of 31 HAADF-STEM images were acquired with tilt increments of 5° over a range of ±75°. Alignment of the data was carried out using the FEI Inspect3D software package. The reconstruction was performed using the “Simultaneous Iterative Reconstruction Technique” (SIRT) with 25 iterations implemented in Inspect3D. Amira (Visage Imaging GmbH) was used for the visualization of the reconstructed volume.

Selected-area electron-diffraction

Crystal structures of the samples were studied by selected-area electron-diffraction (SAED). SAED patterns were measured on a Philips Tecnai 12 electron microscope with an acceleration voltage of 120 kV. Measured two-dimensional patterns were reduced to one dimension by rotationally averaging the patterns around the center. The center was first manually defined and then refined using a down-hill simplex algorithm using the PASAD plugin for the Digital Micrograph software suite.[42]

The algorithm for rotational averaging is as follows: for every pixel in the SAED image, the distance to the center (x, in pixels) is calculated. The pixel brightness (y, arbitrary units) of pixels with the same x are summed. The summed y values are then averaged, by dividing them by the number of pixels with the respective x value. This algorithm was implemented in a custom-made computer program, written in the C++ programming language.

The obtained one-dimensional patterns were calibrated to the sample cation exchanged with $InCl_3$-TOP, of which a usable XRD pattern was obtained (Appendix Figure 1).

Calculated diffraction patterns

Diffraction patterns for a number of crystal structures were calculated by loading the referenced crystal structure data into the Visualization for Electronic and Structural Analysis (VESTA) imaging software [43] (version 3.2.1) and from within VESTA running the RIETAN-FP modelling software (version 2.71) using the default settings.[44]

4. Results and discussion

4.1 Cation exchange in $Cu_{2-x}S$ bifrustums: tuning precursor reactivity

The largest part of this work focusses on cation exchange reactions in $Cu_{2-x}S$ bifrustum nanocrystals (NCs). These particles were chosen as a model system because they are easy to study using transmission electron microscopy (TEM), owing to their size (10 – 15 nm). They show a homogeneous contrast in TEM micrographs and tend to order in three-dimensional superlattices (Figure 11a). They have the low-chalcocite $Cu_{2-x}S$ crystal structure (Figure 11d). Due to the presence of Cu^+ vacancies, compensated for by holes, these particles exhibit a broad plasmonic absorbance band in the near infra-red region (Appendix Figure 2).

As a starting point, we will take the cation exchange (CE) procedure reported in Ref. [14], for the conversion of $Cu_{2-x}S$ nanocrystals (NCs) into $CuInS_2$ (CIS). In this procedure, $Cu_{2-x}S$ NCs are reacted with $InCl_3$-trioctyl phosphine ($InCl_3$-TOP). The use of this single-step precursor couples the cation incorporation and extraction rates, allowing for better control over the exchange rates. When $Cu_{2-x}S$ NCs are reacted with $InCl_3$-TOP at 100°C, they are indeed converted into CIS NCs (Figure 11b). This is confirmed by energy-dispersive X-ray spectroscopy (EDX) measurements (Appendix Figure 3), with a measured Cu:In:S ratio of 1.0:0.81:2.0 (expected CIS composition: Cu:In:S = 1:1:2). Furthermore, selected-area electron diffraction (SAED) shows a transformation from low-chalcocite $Cu_{2-x}S$ (Figure 11a) into wurtzite CIS (Figure 11b). The obtained SAED patterns were rotationally averaged for easier comparison (Figure 11d, e). These show good agreement with reference patterns. The shape of the NCs is well-conserved after the CE reaction. SAED patterns are used to analyse the crystal structure of the particles, instead of X-ray diffraction, because the latter method yielded patterns with a poor signal/noise ratio, making it impossible to accurately determine the crystal structure. After reaction with $InCl_3$-TOP, the broad plasmonic absorbance band is absent from the spectrum. This is an indication that the product NCs no longer possess free charge carriers (holes). A small absorption band is present around λ = 600 nm (Appendix Figure 2), which is consistent with the absorption spectrum of CIS.[33]

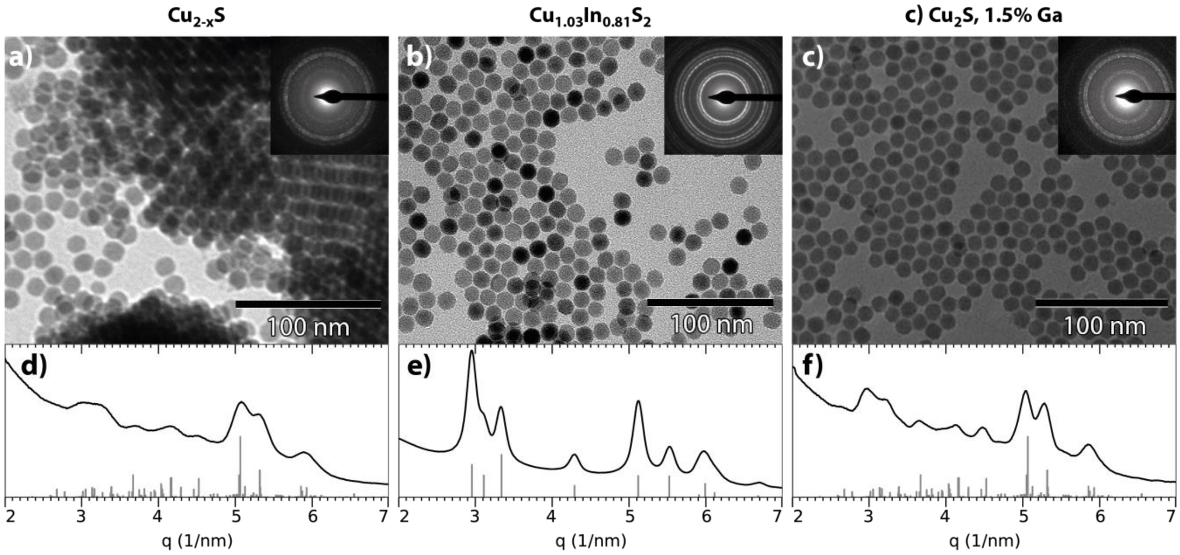

Figure 11. TEM micrographs of (a) $Cu_{2-x}S$ bifrustum nanocrystals, unreacted; (b) $CuInS_2$ bifrustum nanocrystals, obtained by cation exchange reaction at 100°C overnight, with $InCl_3$-TOP, using the nanocrystals shown in (a) as parent nanocrystals; (c) Cu_2S:Ga nanocrystals, after cation exchange reaction at 100°C overnight, with $GaCl_3$-TOP, using the nanocrystals shown in (a) as parent nanocrystals. Top-right insets show SAED patterns of the depicted samples. Bottom panels show rotationally averaged patterns of (d) the pattern shown in (a); (e) the pattern shown in (b); (f) the pattern shown in (c). Grey reference bars are (d, f) calculated patterns based on the crystal structure described in [45]**; (e) patterns directly obtained from JCPDS PDF-card 01-077-9459. Headers give the stoichiometry of the particles as determined with EDX.**

A direct adaptation of the above procedure, using $GaCl_3$-TOP instead of $InCl_3$-TOP, does not convert the $Cu_{2-x}S$ NCs into $CuGaS_2$ (CGS) ones. Instead, only a limited amount of Ga^{3+} is incorporated into the NCs. Quantification of the EDX spectrum (Appendix Figure 4) indicates that the product particles contain only 1.5 atomic % Ga. SAED patterns (Figure 11c,f) show that the NCs still have the low-chalcocite $Cu_{2-x}S$ crystal structure. As in the original cation exchange procedure, the particles have retained their size and shape after the reaction. Analysis by absorption spectroscopy shows that after reaction with $GaCl_3$-TOP, the plasmonic absorption band is absent (Appendix Figure 2). However, no clear features can be discerned, apart from a strong increase in absorbance at shorter wavelengths, starting from $\lambda \approx 500$ nm.

Clearly, the method applied for the conversion of $Cu_{2-x}S$ NCs into CIS NCs by CE cannot be directly applied to the CE of Cu^+ for Ga^{3+}. To further study the influence of the CE precursor on the outcome of CE reactions, two new GaCl3-phosphine complexes were used as precursors. $GaCl_3$ was complexed with diphenyl phosphine (DPP) and triphenyl phosphite (TPP), yielding $GaCl_3$-DPP and $GaCl_3$-TPP, respectively.

Both $GaCl_3$-DPP and $GaCl_3$-TPP appear to exchange Cu^+ for Ga^{3+} in the $Cu_{2-x}S$ parent NCs. This is indicated by EDX results (Appendix Figure 6, 7) which give compositions (Cu:Ga:S = 0.92:1.4:2.0 for $GaCl_3$-DPP and 1.6:1.1:2.0 for $GaCl_3$-TPP) wherein gallium is a major component. The SAED patterns of particles reacted with $GaCl_3$-TPP show a conversion from the low-chalcocite $Cu_{2-x}S$ crystal structure into the meta-stable wurtzite CGS crystal structure (Figure 12c,f), indicating that the exchange was indeed successful.

After reaction with $GaCl_3$-DPP, the nanoparticles have sintered (Figure 12b), explaining the loss of crystallinity observed in the SAED patterns (Figure 12b,e). This aggregation may be due to exchange of the original OA and DDT ligands for the shorter DPP ligand. The latter may be too short to prevent sintering. NCs reacted with $GaCl_3$-TPP have deformed somewhat and have become more polydisperse. Interestingly, intra-NC contrast differences are observed for the sample reacted with $GaCl_3$-TPP (Figure 12c). After reaction with either of the two precursors, the broad plasmonic absorption band is absent in the absorbance spectra (Appendix Figure 8). The particles reacted with $GaCl_3$-DPP show an absorption peak at $\lambda = 350$nm, the nature of which is unknown.

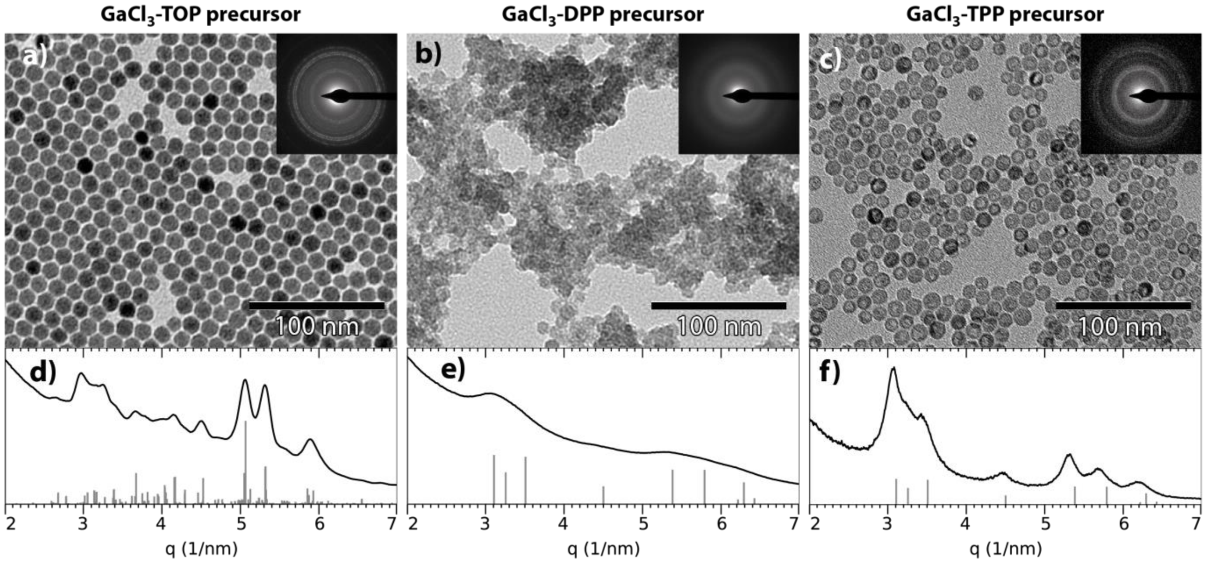

Figure 12. TEM micrographs of (a) Cu_2S:Ga nanocrystals, after reaction at 100°C with $GaCl_3$-TOP, overnight; (c) $CuGaS_2$ nanoparticles, after reaction at 100°C with $GaCl_3$-DPP, for 1h; (c) $CuGaS_2$ nanocrystals, after reaction at 100°C with $GaCl_3$-TPP, for 1h; Top-right insets show electron-diffraction images of the depicted samples. Bottom panels show rotationally averaged patterns of (d) the pattern shown in (a); (e) the pattern shown in (b); (f) the pattern shown in (c). Gray reference bars are calculated patterns based on (a,c) the crystal structure described in [46]**; (b) the crystal structure described in** [45]**.Due to the smaller size of the parent particles used to produce (a) and (b), these particles are smaller than those depicted in (c), because of the a different, smaller, batch of parent nanocrystals.**

The nature of the contrast-difference observed in particles reacted with $GaCl_3$-TPP was investigated using HAADF-STEM and elemental mapping (Figure 13). HAADF-STEM analysis (Figure 13a) shows a similar intraparticle contrast as observed by TEM (Figure 12c). In the elemental mapping of Cu and Ga (Figure 13b,c), this difference in contrast is not as clear. In most NCs, the signal of Cu and Ga are well correlated, indicating that the product NCs have a homogeneous composition. Only few NCs exhibit an inhomogeneous composition (Figure 13b,c, indicated by orange arrows). The discrepancy between the elemental mapping and the contrast difference observed in TEM and HAADF-STEM micrographs may be due to small cavities at the nanocrystal surface or small voids within the NCs.

These results show that the type of precursor can greatly affect the outcome of CE reactions. Use of $GaCl_3$-TOP instead of $InCl_3$-TOP as CE precursor results in incorporation of only a limited amount of Ga^{3+} into the NCs. However, use of $GaCl_3$-DPP or $GaCl_3$-TPP as CE precursor results in a successful exchange of Cu^+ for Ga^{3+}. Since the parent NCs are the same type for all four precursors used, we can conclude that solid-state Ga^{3+} diffusion is not the rate limiting step in these CE reactions. If it were the rate limiting step, CE reactions using $GaCl_3$-DPP or $GaCl_3$-TPP would as unsuccessful as the CE reaction with $GaCl_3$-TOP.

The different results, obtained by reaction with either $InCl_3$-TOP or $GaCl_3$-TOP, thus cannot be attributed to a slower diffusion rate of Ga^{3+}, compared to In^{3+}. Instead, the explanation may be sought in the differences between the stability of the reactants (*i.e.*, the chemical potentials: $\mu_{GaCl3\text{-}TOP}$ and $\mu_{InCl3\text{-}TOP}$) on the one hand, and the stability of the products (*i.e.,* the chemical potentials μ_{CuGaS2} and μ_{CuInS2}) on the other. These four factors influence the position of the equilibrium of the cation exchange reaction, while also influencing the kinetics (a lower chemical potential coincides with a higher activation energy and thus a lower reaction rate).

Hard-soft acid-base theory states that species of comparable chemical hardness (η) have a higher affinity for one another than species with dissimilar chemical hardnesses.[27] Ga^{3+} has a relatively high chemical hardness (η = 17 eV)[27], higher than that of In^{3+} (η = 13 eV)[27]. Tertiary phosphines, on the other hand, are relatively soft ($\eta \approx$ 6 eV)[11]. We thus expect $\mu_{GaCl3\text{-}TOP}$ to be larger than $\mu_{InCl3\text{-}TOP}$, since the chemical hardness of In^{3+} matches that of TOP better.

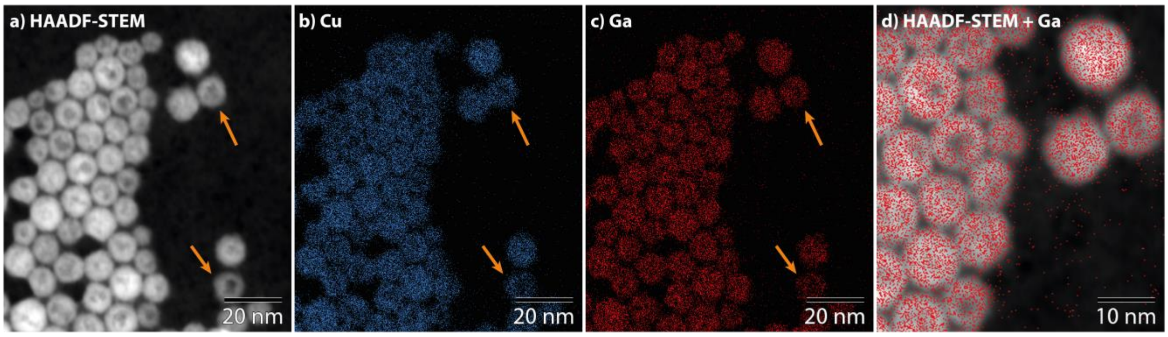

Figure 13. (a) HAADF-STEM image of $CuGaS_2$ nanocrystals, obtained by reacting $Cu_{2-x}S$ bifrustum nanocrystals with $GaCl_3$-TPP at 100°C, for 60 min. (b-d) elemental mapping via EDX of the same sample, with (b) the Cu signal; (c) the Ga signal; (d) enlarged view of the Ga signal overlaid on the HAADF-STEM micrograph. Orange arrows indicate particles that show an inhomogeneous composition.

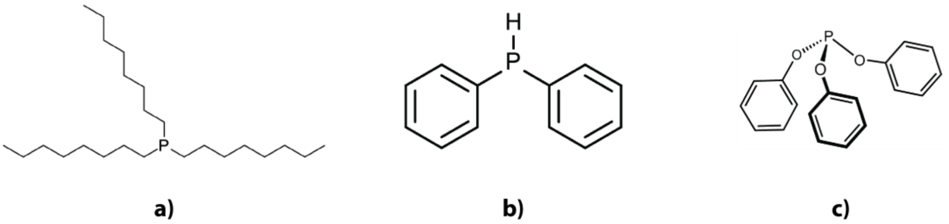

Figure 14. Structure formulae of the three used ligands: (a) trioctyl phosphine (TOP); (b) diphenyl phosphine (DPP); (c) triphenyl phosphite (TPP).

However, we do not observe succesful cation exchange when $GaCl_3$-TOP is used, as one would expect when only $\mu_{GaCl3\text{-}TOP}$ and $\mu_{InCl3\text{-}TOP}$ are taken into account. This suggests that the difference between μ_{CuGaS2} and μ_{CuInS2} may cause the difference between the exchange with In^{3+} and with Ga^{3+}. It appears that the formation of CGS is less favourable than the formation of CIS. To such an extent, in fact, that only a few percent of Cu^+ is exchanged for Ga^{3+}.

The use of DPP or TPP instead of TOP as ligands for $GaCl_3$ appears to greatly affect the outcome of the cation exchange reaction: using the former two molecules as ligands results in a successful exchange of Cu^+ with Ga^{3+}. The three ligands used differ in their size and in the electron-withdrawing nature of their side groups. The side groups of TOP are relatively long alkyl chains, which are poor electron-withdrawing groups (Figure 14a). DPP is a smaller molecule: the phosphorous atom is bound to two phenyl groups and a hydrogen atom (Figure 14b). These phenyl groups are more electron-withdrawing than the alkyl chain side groups of TOP.[47] Finally, TPP is larger than DPP, possessing three phenoxy side groups, which are more electron withdrawing than the phenyl groups in DPP.[47] The differences in electronic properties of the three ligands result in a trend in electron density *ρ* on the phosphorous atom[47]:

$$\rho_{TPP} < \rho_{DPP} < \rho_{TOP} \tag{3}$$

Previously, this trend was used to tune the reactivity of chalcogenide-phosphine complexes used in the synthesis of nanocrystals.[47] We will assume that in the three complexes used ($GaCl_3$-TOP, GaCl3-DPP and $GaCl_3$-TPP), the gallium atom is directly bound to the phosphorous atom (as is the case for $GaCl_3$ complexed with triethyl phosphine[48] and triphenyl phosphine[49]).

The electron density *ρ* on the phosphorous atom is tentatively proposed to influence the strength of the Ga-P bond, with larger *ρ* resulting in a stronger Ga-P bond. The trend in reactivity of the $GaCl_3$-phosphine complexes is then similar to the trend in reactivity of chalcogenide-phosphine complexes,[47] with higher *ρ* resulting in lower $\mu_{GaCl3\text{-}L}$ (*L* = TOP, DPP, TPP):

$$\mu_{GaCl3\text{-}TOP} < \mu_{GaCl3\text{-}DPP} < \mu_{GaCl3\text{-}TPP} \tag{4}$$

This trend in chemical potential explains the different results obtained with the three different ligands. Higher $\mu_{GaCl3\text{-}L}$ favours the reaction both thermodynamically and kinetically, thus reactions with $GaCl_3$-DPP and $GaCl_3$-TPP yield exchange Cu^+ for Ga^{3+}. On the other hand, $\mu_{GaCl3\text{-}TOP}$ is relatively small, thus only few Cu^+ ions are exchanged with Ga^{3+} when $GaCl_3$-TOP is used as precursor.

Like the transformation of $Cu_{2\text{-}x}S$ into CIS nanocrystals reported on above, the exchange of Cu^+ for Ga^{3+}, using $GaCl_3$-DPP or $GaCl_3$-TPP, occurs only partially. Instead of Ga_2S_3, CGS nanocrystals are produced. For the exchange of Cu^+ for In^{3+}, this partial exchange was previously explained by the incompatibility of the anion sublattice of low-chalcocite $Cu_{2\text{-}x}S$ and spinel In_2S_3.[33] For a complete transformation into In_2S_3, the anionic sublattice would have to rearrange from a hexagonal close-packed structure to a face-centered cubic one (corresponding to a dislocation of 58% of a S-S interatomic distance)[33]. The associated energy barrier for such a transformation is too high for the mild reaction conditions, thus the exchange stops when the intermediate wurtzite CIS structure is reached.

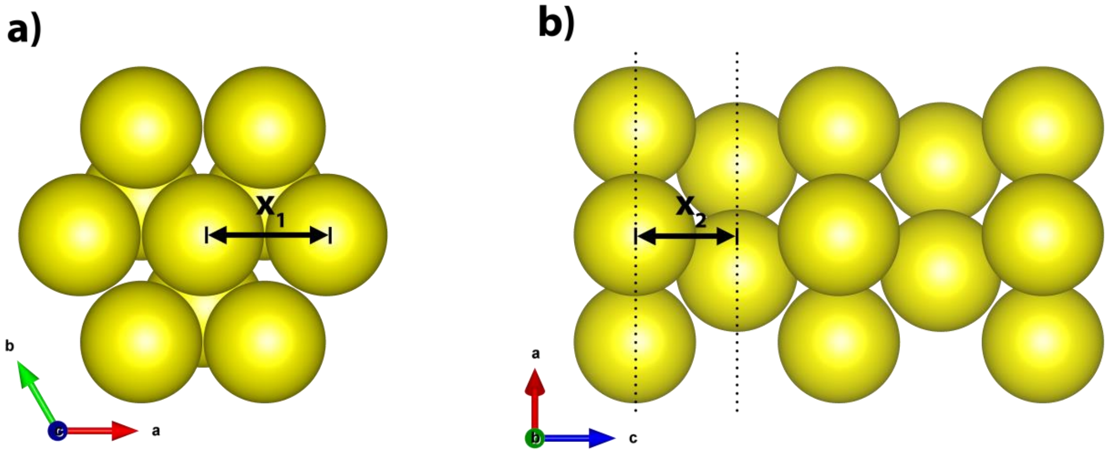

Figure 15. Images depicting the anionic sublattice (S^{2-} anions) of $CuGaS_2$, (a) viewed from the [001] direction; (b) viewed from the [010] direction. x_1 denotes the interatomic distance within the hexagonal layers, while x_2 denotes the distance between the layers. Images were produced based on the crystal structure described in Ref. [46]**.**

For the present partial Cu^+ for Ga^{3+} cation exchange, this argument may not apply. Low-chalcocite $Cu_{2-x}S$, wurtzite CGS and the stable form of bulk Ga_2S_3, monoclinic α'-Ga_2S_3, all have an hcp anionic sublattice [45,46,50]. The difference between these sublattices can be quantified by the difference in the interatomic distance within the hexagonal layers, x_1, and the difference in interlayer distance, x_2 (Figure 15). In both the conversion of low-chalcocite $Cu_{2-x}S$ into wurtzite CGS and into α'-Ga_2S_3, a contraction of the anion lattice is necessary. The amount of contraction differs only slightly between the two conversions: in the former, the contraction is 5.92% within layers and 8.98% between layers, in the latter the contractions are 6.42% and 11.35%, respectively. Although the extra contraction required for the conversion into monoclinic α'-Ga_2S_3 (0.50 and 2.37 percentage point for the contraction within layers and between layers, respectively) is small, the energy barrier corresponding to this contraction may actually be large, since the atoms may be forced into an unfavourable configuration.

The values of the contractions listed above indicate that CGS is likely to be a metastable intermediate phase in the transformation of $Cu_{2-x}S$ into α'-Ga_2S_3 (*i.e.*, to reach the α'-Ga_2S_3 phase, the system first has to go through the wurtzite CGS phase). Since the exchange does not proceed further than the wurtzite CGS phase, we can infer that this phase represents a local energy minimum, with the activation barrier for full conversion into α'-Ga_2S_3 too high to overcome under the present reaction conditions.

4.2 Cation exchange in $Cu_{2-x}S$ bipyramids

The results of the previous section show that a successful cation exchange procedure for one element is not necessary suitable for another element. In this section, we will see that the NC morphology is also of great influence, and that diffusion can play a large role in cation exchange reactions. Instead of bifrustum $Cu_{2-x}S$ NCs, we will now discuss the Cu^+ for Ga^{3+} cation exchange in bipyramid $Cu_{2-x}S$ NCs. These NCs are larger than the previously discussed bifrustum NCs (bipyramid length ≈ 35nm, width ≈ 25nm; bifrustum diameter ≈ 10 - 15 nm) and also have the low-chalcocite $Cu_{2-x}S$ crystal structure.[40] These bipyramid particles differ from the bifrustum particles in their capping ligands: for the synthesis of the bifrustum NCs, dodecanethiol (DDT) and oleic acid (OA) are used. For the synthesis of the bipyramid particles, the used ligands are DDT and oleyl amine (OLAM).

Before cation exchange, these particles show a homogeneous contrast in TEM micrographs (Figure 16a). After reacting with $GaCl_3$-TOP at 200°C, the particles have retained their shape. Interestingly, the contrast within the particles is, for a number of particles, heterogeneous. In some particles the center is darker than the tips (Figure 16b). Elemental analysis with EDX (Appendix Figure 5) shows that the sample contains less Ga than expected for CGS (measured elemental composition: Cu:Ga:S=2.38:0.58:2.00, expected for CGS: 1:1:2), indicating that the cation exchange reaction did not proceed fully. Nonetheless, the X-ray diffraction (XRD) pattern of the product NCs is dominated by peaks that can be attributed to wurtzite CGS (Figure 16c), indicating that a transformation of low-chalcocite $Cu_{2-x}S$ into wurtzite CGS has taken place. Some peaks in the XRD pattern do not correspond to wurtzite CGS and may instead be attributed to low-chalcocite $Cu_{2-x}S$ (Figure 16c). The combination of the EDX and XRD results suggests that the CE may have yielded NCs composed of Ga-rich wurtzite CGS domains, and Ga-poor low-chalcocite $Cu_{2-x}S$ domains (possibly doped with Ga).

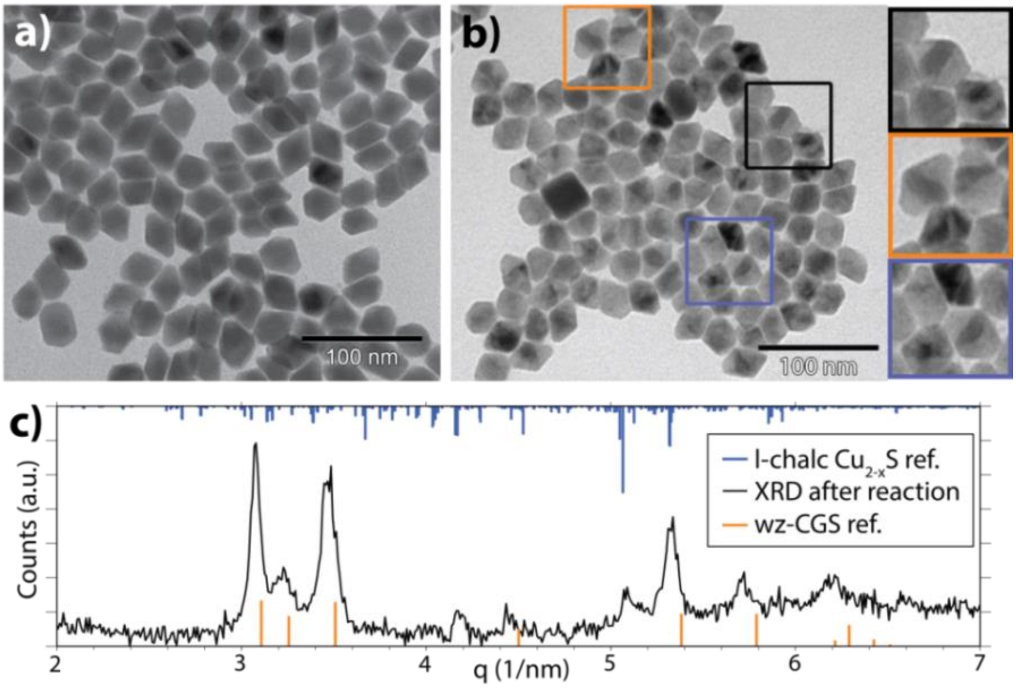

Figure 16. TEM micrographs of (a) $Cu_{2-x}S$ bipyramid parent nanocrystals; (b) $Cu_2S/CuGaS_2$ bipyramid nanocrystals obtained by reacting $Cu_{2-x}S$ bipyramid parent nanocrystals with $GaCl_3$-TOP at 200°C, overnight. Right insets correspond to highlighted areas in (b) and are centered on nanocrystals showing clear intraparticle contrast. (c) XRD pattern of the sample depicted in (b). (top, blue) reference bars correspond to a low-chalcocite $Cu_{2-x}S$ reference [45], **(bottom, orange) reference bars correspond to a wurtzite $CuGaS_2$ reference** [46].

To verify if this is indeed the case, as well as to elucidate the origin of the observed intraparticle contrast in TEM, the elemental composition of a single product NC was analysed with EDX. High-angle annular dark-field scanning transmission electron microscopy (HAADF-STEM) micrographs of the NC show contrast within the NC, in agreement with the TEM micrographs (Figure 17a,b). The elemental composition of this NC was measured across its length axis, by performing an EDX line scan (Figure 17c). This line scan shows that sulphur is distributed relatively homogenously throughout the NC (due to the bipyramid shape, the amount of sulphur is expected to be largest at the NC center and lower at the tips), while Cu appears to be present mostly in the center of the particle, and Ga mostly in the tips. EDX area-scans of the NC tips and center yield results that agree with the line scan: the tips are Ga-rich (17.4 and 12.9 atomic %), while the center contains only a small portion of Ga (2.3 atomic %) (Figure 17d,e).

Analysis by TEM and EDX thus indicates that after CE with $GaCl_3$-TOP at 200°C, some bipyramid NCs have a heterogenous composition, with Ga-rich tips and a Cu-rich center. The existence of peaks attributed to low-chalcocite $Cu_{2-x}S$ in the XRD pattern indicates that some low-chalcocite crystalline domains remain. The heterogenous composition of the NCs after the reaction suggests that these low-chalcocite domains may coincide with the Cu-rich core of the NCs, while the wurtzite crystalline domains may correspond to the Ga-rich NC tips.

These $Cu_{2-x}S$ bipyramid NCs are partially converted into CGS by reacting with $GaCl_3$-TOP, while the same procedure, at a lower reaction temperature, incorporated only 1.5% Ga into the bifrustum $Cu_{2-x}S$ NCs. This suggests that the NC shape and reaction temperature are important factors in this CE reaction. The tips of the bipyramid particles are a high-energy surface (due to their large surface area). They are thus the most reactive (*e.g.,* the activation energy is locally lower) parts of the NC. This may locally tilt the thermodynamic balance in favour of transformation into CGS, as well as increase exchange rates at these surfaces (due to a decreased energy barrier). This allows the cation exchange to occur at the tips of these NCs. The higher reaction temperature (200°C, compared to 100°C) may also help to overcome the required activation energy for the CE reaction. $Cu_{2-x}S$ bipyramid NCs were also reacted with $GaCl_3$-TOP at 100°C. However, elemental analysis on these particles was not yet performed. Therefore, it is not yet possible to determine if the higher reaction temperature, the NC shape, or a combination of both leads to successful CE of Cu^+ for Ga^{3+}.

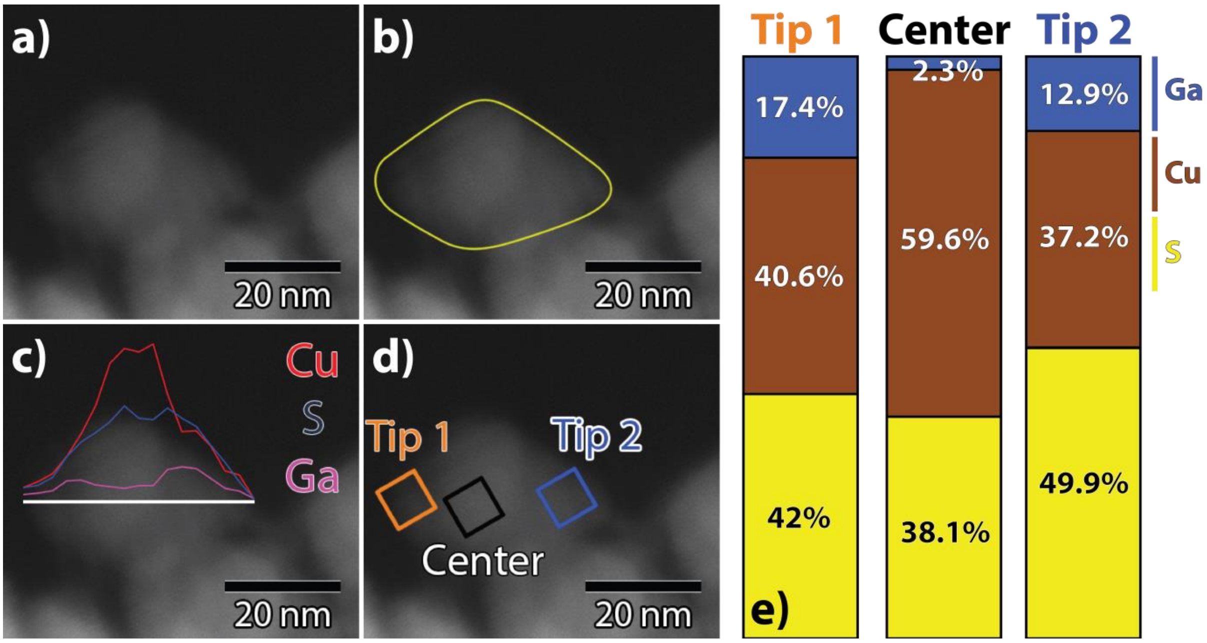

Figure 17. (a-d) HAADF-STEM micrographs of a $CuGaS_2/Cu_2S/CuGaS_2$ bipyramid nanocrystals obtained by reacting $Cu_{2-x}S$ bipyramid nanocrystals with $GaCl_3$-TOP at 200°C overnight; (b) a single bipyramid nanocrystal outlined in yellow; (c) EDX linescan of the outlined nanocrystal, red: Cu signal, blue: S signal, pink: Ga signal; (d) location of EDX area scans indicated on the TEM micrograph; (e) graph representing the atomic % of Cu, Ga and S, at the three highlighted locations.

A combination of two factors explains the heterogeneous composition of the product NCs. Due to the relatively large reactivity of the bipyramid tips, the cation exchange of Cu^+ with Ga^{3+} will take place at both ends of the NC (Figure 18a). Ga^{3+} then diffuses inward, while Cu^+ diffuses outward, resulting in an inward-moving reaction front (Figure 18b,c). Secondly, the diffusivity of Ga^{3+} is relatively low, even at a reaction temperature of 200°C. If the diffusion rate of Ga^{3+} were fast, the product NCs would not have a heterogeneous composition, but be composed of a graded alloy.[26]

There are multiple possibilities for why the NCs do not fully exchange into CGS. One possible reason is strain, induced by the inward-moving reaction front. Recently, Ha *et al.* reported on the formation of similarly heterostructured NCs via cation exchange.[31] They showed that strain, due to lattice mismatch between the reaction front and the unreacted center, increased as the reaction front moved inward. At one point, the strain presents an energy barrier which is too high to overcome, stopping inward diffusion and thus the cation exchange (Figure 18d). However, the contraction required for the conversion of low-chalcocite $Cu_{2-x}S$ into wurtzite $CuGaS_2$ is small (5.92% within S^{2-} hexagonal layers and 8.98% between layers). The successful CE of Cu^+ for Ga^{3+} in bifrustum $Cu_{2-x}S$ NCs, using $GaCl_3$-DPP and $GaCl_3$-TPP, indicates that this lattice mismatch is small enough to overcome during the CE reaction. Strain may thus not be the reason for the observed formation of heterostructured NCs.

Another reason for the incomplete conversion into wurtzite $CuGaS_2$ may be that the CE reaction is simply not finished yet. Since diffusion is a stochastic process, the diffusion rates may not be equal for all NCs. Thus, in some NCs the reaction front may move inward relatively fast, yielding NCs with a homogeneous contrast in TEM, while in other NCs, the front may move in relatively slow, yielding a heteronanocrystal.

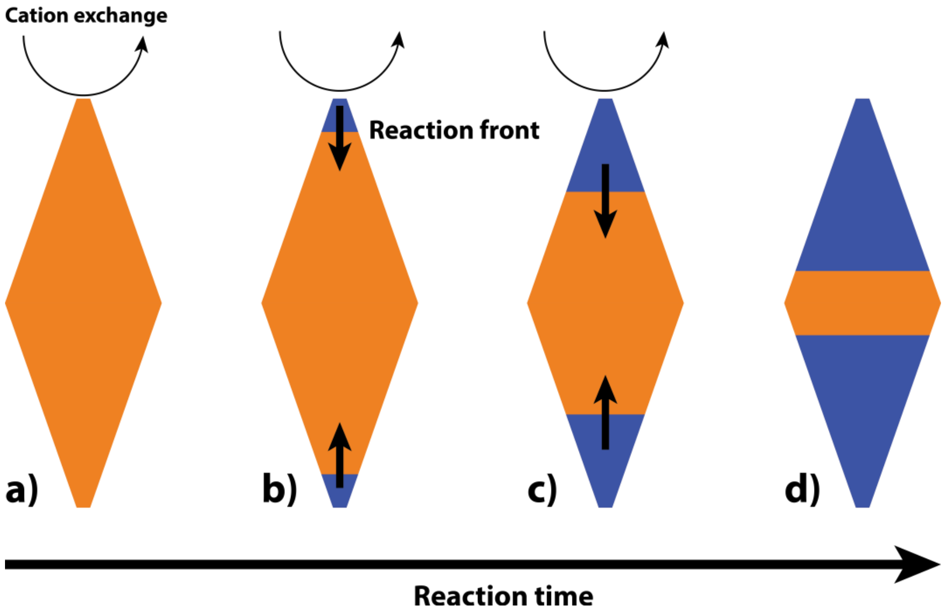

Figure 18. Proposed reaction progression for cation exchange of $Cu_{2-x}S$ bipyramid nanocrystals with $GaCl_3$-TOP: (a) cation exchange occurs at the tips of the NCs. (b) the tips of the NC become Ga-rich, a reaction front is formed; (c) the reaction front moves inward, until (d) the reaction is quenched or, (possibly) the strain induced in the crystal lattice poses an energy barrier which is too large to be overcome.

4.3 Formation of hollow nanocrystals from $Cu_{2-x}S$ bifrustum nanocrystals

In this section, we will discuss the hollowing of $Cu_{2-x}S$ bifrustum nanocrystals, by reacting with $GaCl_3$. When $Cu_{2-x}S$ bifrustum NCs are reacted with $GaCl_3$ at 30°C, the reaction proceeds at a much slower rate than the previously discussed cation exchange reactions. This allows for the study of the progression of the reaction by taking samples at different reaction times. TEM micrographs of these samples show the formation of a small bright spot in the particles (Figure 19b), which grows over time (Figure 19c-f). As the reaction continues, dark spots become visible within the particles (Figure 19e, f). Analysis by SAED indicates that after reaction times of 120 and 300 minutes, the particles still have the low-chalcocite $Cu_{2-x}S$ crystal structure (Figure 20). Interestingly, EDX analysis of samples reacted for 120 and 300 minutes shows that the Ga contents increases after longer reaction times. Particles reacted for 120 minutes contain 4 atomic % Ga (Appendix Figure 9), while particles reacted for 300 minutes contain 20 atomic % Ga (Appendix Figure 10).

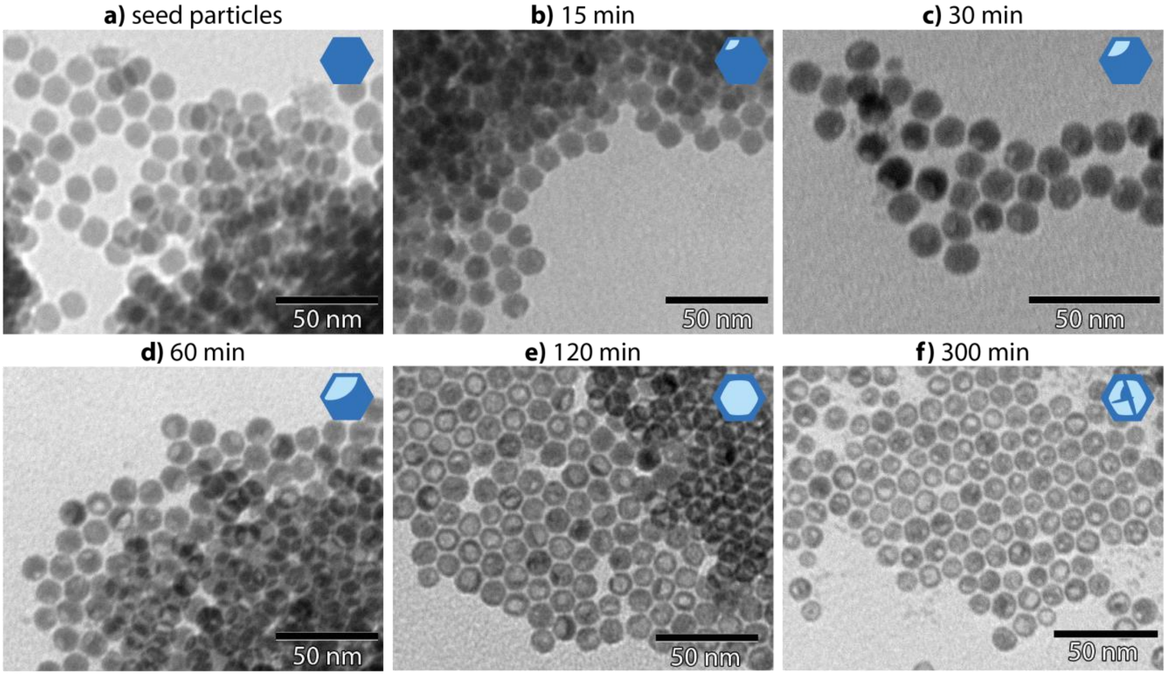

Figure 19. TEM micrographs of $Cu_{2-x}S$ bifrustum nanocrystals, (a) before reaction (parent nanocrystals), and after reaction at 30°C with $GaCl_3$, for (b) 15 min, (c) 30 min, (d) 60 min, (e) 120 min, (f) 300 min.

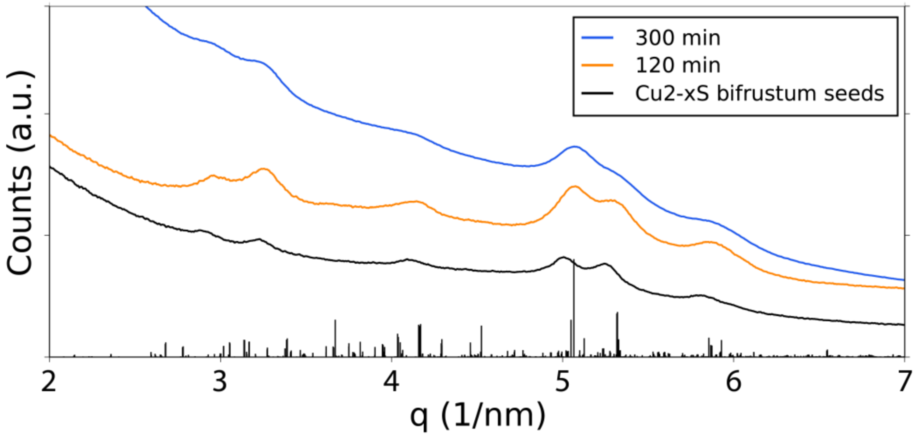

Figure 20. Rotationally averaged selected-area electron diffraction patterns of (bottom, black) $Cu_{2-x}S$ bifrustum parent nanocrystals, before reaction and particle reacted at 30°C with $GaCl_3$ for (middle, orange) 120 min, (top, blue) 300 min. These patterns were measured of samples corresponding to (bottom, black) Figure 19a; (middle, orange) Figure 19e; (top, blue) Figure 19f.

The bright regions observed within the particles in TEM micrographs may indicate the presence of other species with low contrast, or a local deficiency of material (*i.e.*, a void or a cavity). To determine the nature of this region and its position within the particles, HAADF-STEM tomography was employed. Visualisations of 3-D reconstructed volumes of NCs (Figure 21) show that after a reaction time of 15 minutes, a small dip is present in some of the particles (Figure 21a). After longer reaction times, a cavity is present (Figure 21b,c). In some cases, particles contain voids which are not connected to the surface of the particle (Figure 21c, indicated by red arrow). Orthoslices of the reconstructed volumes indicate the presence of cavities and voids within the NCs (Figure 21d-f). These images suggest that the bright regions observed in the TEM micrographs coincide with cavities within the particles, which form at the surface of the NCs and grow inwards over time.

The HAADF-STEM tomography results do not explain the presence of Ga in these particles, as measured by EDX. Thus, elemental mapping and HAADF-STEM imaging was performed on particles reacted for 120 and 300 minutes, to study the presence of Ga in more detail. HAADF-STEM micrographs of $Cu_{2-x}S$ particles reacted for 120 minutes show a similar contrast difference as in TEM, with a clear contrast difference between the middle and the outer parts of the particles (Figure 22a).

Differences in Cu-contents observed by elemental mapping (Figure 22b) correlate well with the HAADF-STEM analysis, with dark regions in the micrograph coinciding with regions with low Cu content. Ga appears to be present in only a small quantity, at positions which correlate with darker regions in the HAADF-STEM micrograph (Figure 22c, d). HAADF-STEM tomography indicates that these positions correspond to cavities or void within the particles. Ga is thus presumably present at the inner surface of the voids within the nanoparticles.

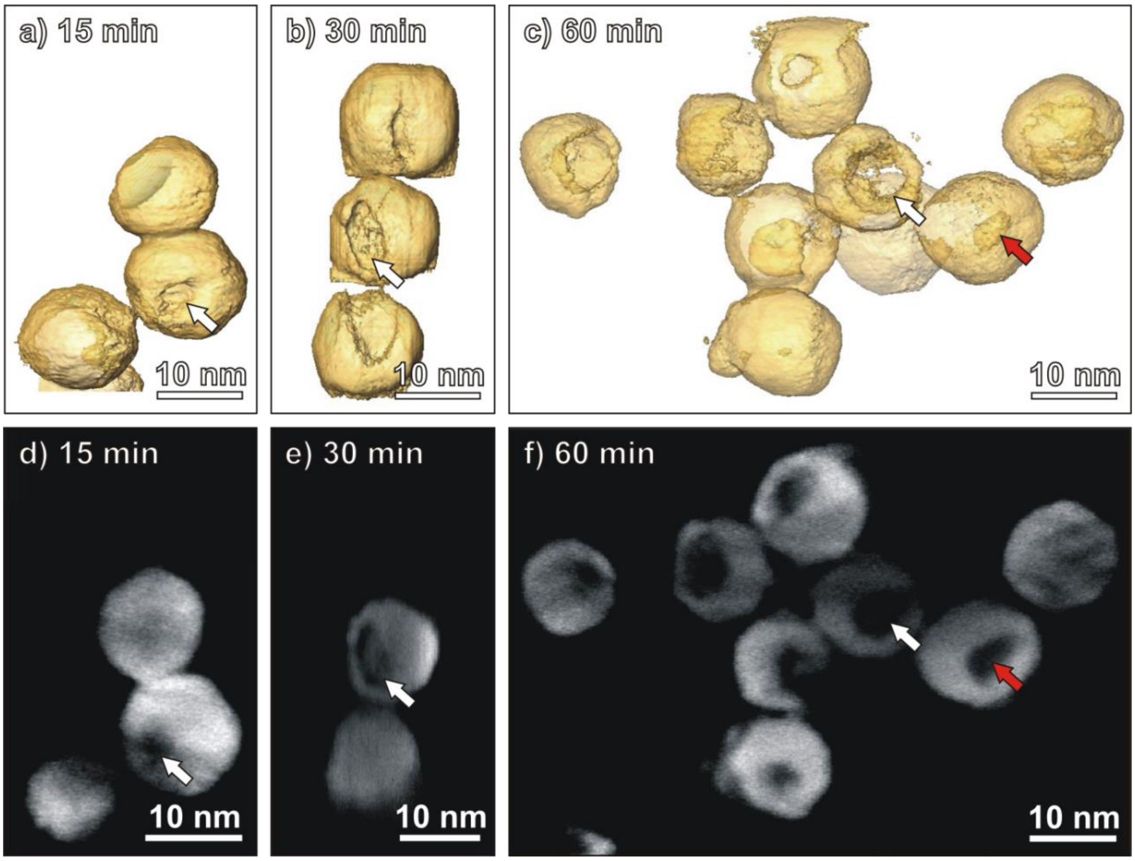

Figure 21. Visualizations of 3-D reconstructions of the $Cu_{2-x}S$ bifrustum nanocrystals after reaction at 30°C with $GaCl_3$ for (a) 15 min; (b) 30 min; (c) 60 min. (d-f) orthoslices through the 3-D reconstructions: (d) orthoslice through (a); (e) orthoslice through (b); (f) orthoslice through (c). White arrows indicate cavities connected to the nanocrystal surface, red arrows indicate voids not connected to the nanocrystal surface.

HAADF-STEM micrographs of particles reacted for 300 minutes have less intraparticle contrast compared to the particles reacted for 120 minutes (Figure 22e). Interestingly, the elemental mapping of Cu in these particles still shows a heterogeneous distribution, similar to the one observed for the sample reacted for 120 minutes (Figure 22f). Gallium is present mostly at the center of the particles, at positions coinciding with a low concentration of Cu (Figure 22g,h). Some particles have lost their original bifrustum shape, and have segregated into a Cu-rich and a Ga-rich region (Figure 22e-h, indicated by orange arrows). The presence of Ga at the center of the particles explains the solid appearance of the particles in HAADF-STEM micrograph: the lack of Cu is compensated by the presence of Ga.

Quantification of the elemental composition in Ga-poor 'shell' regions and Ga-rich 'core' regions (Figure 23) shows an increase in the Ga contents over time: after a reaction time of 120 minutes, the Ga-poor regions contain 0.8 at.% Ga and the Ga-rich regions contain 15 at.% Ga. After 300 minutes, the Ga-contents are 6 and 30 at.%, respectively.

In order to determine the nature of the Ga present in the center of the particles, HRTEM micrographs were recorded of the nanocrystals reacted for 300 minutes. These images show that the nanocrystals consist of multiple crystalline domains (Figure 24a). The small size of these domains, and overlap of different domains, makes it difficult to determine the crystal structure based on these images. However, some particles show contrast patterns which are suitable for analysis by fast-fourier transform (FFT) (Figure 24b-e). The FFT pattern of one particle could be matched well to both wurtzite CGS and monoclinic α'-Ga_2S_3 (Figure 24c). It was not possible to match this pattern to low-chalcocite $Cu_{2-x}S$, indicating that the analyzed particle contains either a wurtzite CGS or a monoclinic α'-Ga_2S_3 crystalline domain. The FFT pattern of another particle could be matched well to low-chalcocite $Cu_{2-x}S$ (Figure 24e), while no match could be found for either wurtzite CGS or monoclinic α'-Ga_2S_3 crystalline, indicating that this particle contains a low-chalcocite $Cu_{2-x}S$ crystalline domain.

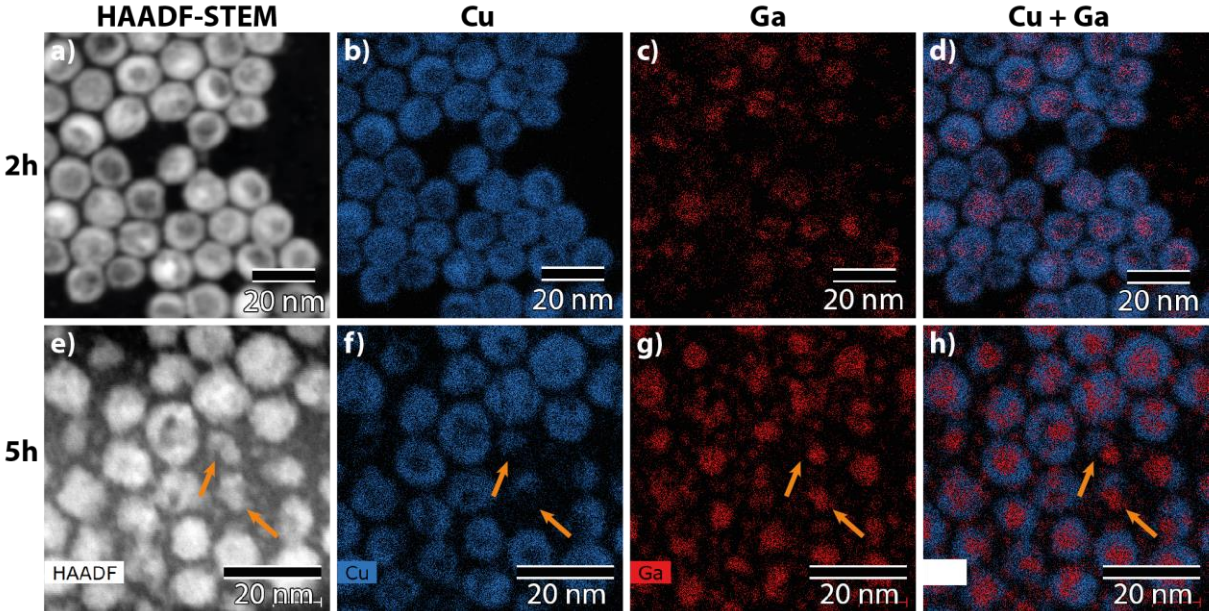

Figure 22. HAADF-STEM micrographs of $Cu_{2-x}S$:Ga nanoparticles, after reaction with $GaCl_3$ (a) for 120 min; (e) for 300 min. Elemental mapping of $Cu_{2-x}S$:Ga nanoparticles, after reaction with $GaCl_3$ for 120 min: (b) Cu; (c) Ga; (d) Cu and Ga. Elemental mapping of $Cu_{2-x}S$:Ga nanoparticles, after reaction with $GaCl_3$ for 300 min: (f) Cu; (g) Ga; (h) Cu and Ga. Orange arrows indicate nanoparticles which composition shows a segregation between a Cu-rich and a Ga-rich region.

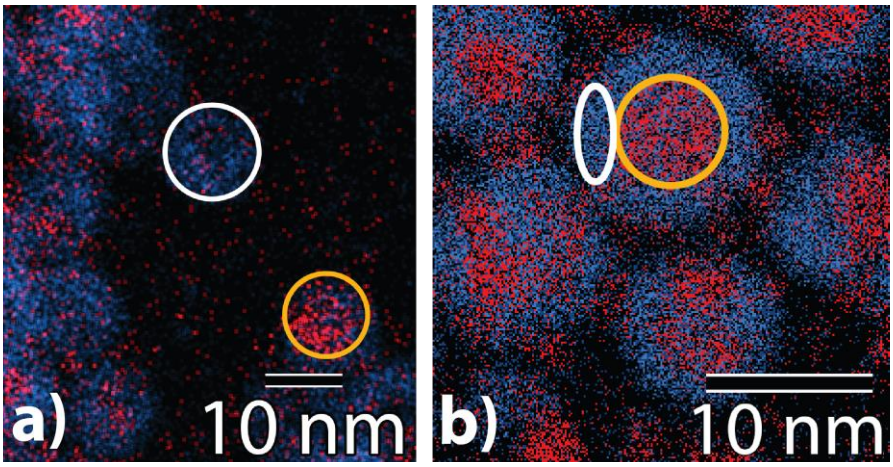

Figure 23. Elemental mapping images of $Cu_{2-x}S$:Ga nanoparticles, after reaction with $GaCl_3$ for (a) 120 min; (b) 300 min. Red colour indicates the Ga signal, blue indicates the Cu signal. White ovals indicate the Ga-poor areas of which the elemental composition was quantified, orange ovals indicate the Ga-rich areas of which the elemental composition was quantified.

While the SAED patterns on the nanocrystals reacted for 300 minutes indicated these particles have the low-chalcocite crystal structure (Figure 19g), crystalline domains of another crystal structure are observed in HRTEM micrographs. This is an indication that crystalline domains, which have a crystal structure other than low-chalcocite $Cu_{2-x}S$, constitute only a small portion of the total number of domains. Thus, their contribution to the SAED patterns is small and hard to distinguish from the larger low-chalcocite contribution.

The formation of voids within NCs which are transformed from one phase into another is often attributed to the nanoscale Kirkendall effect.[51] In the case of CE, this entails the exchange of cations at the nanocrystal surface, accompanied by the diffusion of the original cations from the center of the particle towards the surface. When the out-going rate of the native cations is higher than the in-going rate of the new ones, a void is left at the center of the particle. Mu *et al*. recently reported on such a system, where hollow CIS nanodisks were formed from solid $Cu_{2-x}S$ ones through Cu^+ for In^{3+} cation exchange [30]. Characteristic of this mechanism is the formation of a cavity on the inside of the NCs, induced by outward diffusion of the native cations.[52] In our system, the voids predominantly grow from the surface of the nanocrystal, instead of from the center. This is an indication that, although similar, the reaction mechanism differs from the previously reported one.[30]

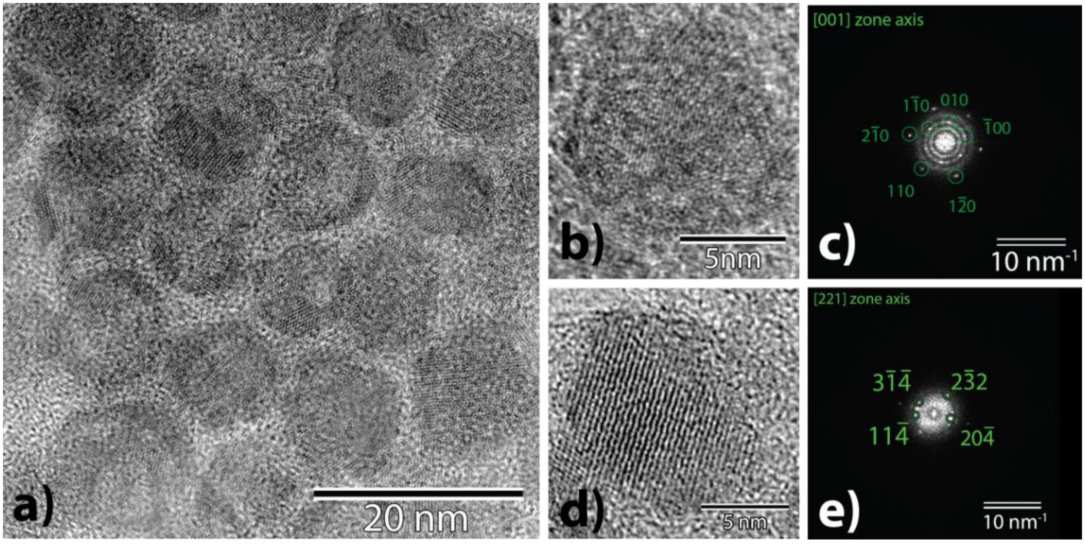

Figure 24. (a,b,d) HRTEM micrographs of nanocrystals obtained by reaction with $GaCl_3$ at 30°C for 300 min. (c) FFT of (b). This pattern could be matched both to monoclinic α'-Ga_2S_3 and wurtzite $CuGaS_2$. The depicted indexation was performed based on the wurtzite $CuGaS_2$ structure, as described in [46]. **(e) FFT of (d). This pattern matched well with the low-chalcocite $Cu_{2-x}S$ crystal structure reported in** [45] **and was indexed accordingly.**

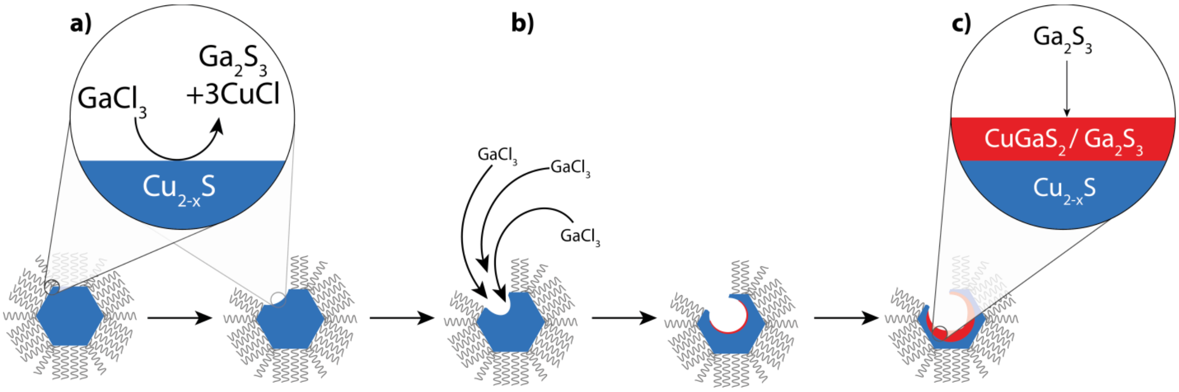

Figure 25. Schematic depicting the proposed reaction progression for $Cu_{2-x}S$ bifrustum nanocrystals reacting with $GaCl_3$: (a) Cu^+ is extracted from the nanocrystal surface, at a rate too high for outward diffusion to keep up, inducing extraction of S^{2-}; (b) due to the depletion of $GaCl_3$ at the original reaction location, a diffusion flow of $GaCl_3$ is induced towards the initial reaction location; (c) Ga-containing species (depicted here as Ga_2S_3) reach a saturation concentration and nucleate inside the nanocrystal, wurtzite CGS and/or monoclinic α'-Ga_2S_3 is formed in the nanocrystal.

The formation of a cavity from the NC surface inward can be explained by an inbalance in the cation incorporation and extraction rates: a high rate of extraction and a low rate of incorporation will lead to depletion of Cu^+ from the NC lattice. If the diffusion of Cu^+ were faster than the extraction of Cu^+, one would expect the formation of a cavity in the center of the NC, as described in.[30] However, if the Cu^+ extraction rate is too fast for the Cu^+ out-diffusion to keep up, the NC surface is depleted of Cu^+ cations, before they can be replaced with outward-diffusing Cu^+. This may induce the extraction of anions from the NC lattice (for example, by Ga^{3+}), in order to keep the NC charge balanced (Figure 25a). Our experiments suggest that this imbalance between the Cu^+ extraction rates and the Cu^+ out-diffusion rates is larger at the corners of the NC, probably due to their higher reactivity. This prevents the dissolution of the NC from the surface inwards, because the reaction then becomes primarily concentrated in the freshly exposed surfaces. Moreover, the fast reaction at the NC surface locally depletes $GaCl_3$, inducing a diffusion flow towards the initial location of reaction (Figure 25b).

Over time, the amount of Ga in the NCs increases. Moreover, the presence of wurtzite CGS or monoclinic α'-Ga_2S_3 is indicated by HRTEM analysis. This suggests that over time, Ga-containing species nucleate and grow on the surface of the cavities in the NCs (Figure 25b,c).

Hollowing of the $Cu_{2-x}S$ bifrustum nanocrystals was not observed when $GaCl_3$-phosphine complexes were used as cation exchange precursors. This suggests that $GaCl_3$, or, more precisely, Cl^-, acts as Cu^+ extracting agent. The phosphine acts as an inhibitor, making $GaCl_3$ less reactive. The CE rates at the surface are thus slowed down when $GaCl_3$ is complexed with a phosphine. This allows the solid-state Cu^+ diffusion to keep up with the CE at the NC surface, thus preventing hollowing of the NCs.

5. Conclusion

Results presented in this work show that there are a number of factors which influence cation exchange reactions. Direct adaptation of a cation exchange procedure (developed for the conversion of $Cu_{2-x}S$ nanocrystals into $CuInS_2$ ones) for cation exchange of Cu^+ for Ga^{3+} in $Cu_{2-x}S$ bifrustum nanocrystals, yielded nanocrystals with only 1.5 atomic % Ga. This indicates that the cation types which are exchanged influence the reaction outcome. Successful partial cation exchange reactions of Cu^+ for Ga^{3+} using $GaCl_3$-DPP and $GaCl_3$-TPP as precursors indicate that the Ga-P bond dissociation is the rate-limiting step in this exchange, not the solid-state diffusion of gallium.

The higher reactivity of $GaCl_3$-DPP and $GaCl_3$-TPP, compared to $GaCl_3$-TOP, is attributed to the more electron-withdrawing nature of the side groups of DPP and TPP. These side groups withdraw electron density from the phosphorous atom, which is proposed to weaken the Ga-P bond.

Reaction of bipyramid $Cu_{2-x}S$ nanocrystals with $GaCl_3$-TOP, at a higher reaction temperature, results in partial cation exchange of Cu^+ for Ga^{3+}. The cation exchange appears to take place at the surface of the bipyramid tips. Due to their high surface/volume ratio, the tips have a high-energy surface, resulting in a lower activation energy for cation exchange at these positions. The combination with a higher reaction temperature allows for the exchange of Cu^+ for Ga^{3+} at these sites. The heterogeneous composition of the nanocrystals, as indicated by TEM, XRD and EDX analyses, is attributed to the low diffusion rate of Ga^{3+} in $Cu_{2-x}S$. This results in a slow, inward-moving reaction front. Due to the stochastic nature of diffusion, the speed at which this front moves inward is not equal for all NCs, resulting in some particles being exchanged further than others.

Reacting bifrustum $Cu_{2-x}S$ NCs with $GaCl_3$, without additional ligands, leads to hollowing of the nanocrystals. This occurs, as indicated by HAADF-STEM tomography, by formation of cavities at the surface of the nanocrystals. The hollowing is proposed to occur because the rate of cation exchange at the nanocrystal surface is too high for the solid-state diffusion rate of Cu^+ to keep up. This results in an unstable, Cu^+-deficient surface. The charge on the nanocrystal is then balanced by expulsion of S^{2-}. In all nanocrystals, the formation of only a single cavity is observed. This is attributed to the induction of a diffusion flow of $GaCl_3$ to the initial reaction location, due to local depletion of $GaCl_3$ by the fast cation exchange reaction. After longer reaction times, the amount of Ga within the particles increases, and a distinct Ga-rich core and Ga-poor shell can be observed using elemental mapping. From HRTEM analysis it appears Ga is present in form of either wurtzite $CuGaS_2$ or monoclinic α'-Ga_2S_3. It is proposed that this increase in Ga-content is due to condensation of Ga-containing species.

6. Outlook

The results presented in this work provide more insight into cation exchange reactions in $Cu_{2-x}S$ nanocrystals. Although this research may answer questions, it also sparks new ones. In this section, a number of possible future studies are proposed, which may provide more insight into cation exchange reactions (CE), or which may yield nanocrystals (NCs) with interesting compositions and optical properties.

Further analyses related to presented work

The presented work can be expanded upon with additional analyses. For example, $Cu_{2-x}S$ nanocrystals reacted with $GaCl_3$-TOP were found to contain 1.5 atomic % Ga. It is not presently known if this gallium is present at the nanocrystal surface, or is incorporated into the crystal lattice. To this end, elemental mapping may provide more insight.

$GaCl_3$-TOP, $GaCl_3$-DPP and $GaCl_3$-TPP were used as cation exchange precursors in this work. It is assumed that these compounds are present as organometallic complexes in solution. However, the exact nature of these complexes is not known. For example, the extent to which these complexes dissociate in solution. Moreover, the reactivity of these precursors was inferred from the electron-density on the phosphorous atom, which is a rather crude method. Computational methods, such as density functional theory (DFT), could shed more light on the reactivity of these precursors.

The bipyramid particles show a heterogeneous composition, with Ga-rich tips and a Ga-poor center. XRD analysis indicates the tips may coincide with wurtzite CGS, while the center coincides with low-chalcocite $Cu_{2-x}S$. High-resolution TEM (HRTEM) may be useful in determining the crystal structure of the bipyramid tips and center. By reacting the bipyramids with $GaCl_3$-TOP for shorter reaction times, the progress of the reaction may be followed, allowing to check if the proposed reaction progression is correct.

The nature of the Ga present in the bifrustum nanocrystals, obtained by reaction with $GaCl_3$, is not yet known. The HRTEM analysis points to the presence of wurtzite CGS. However, it is difficult to draw definite conclusions from the HRTEM micrographs, because individual particles consist of multiple crystalline domains. Electron-energy loss spectroscopy (EELS) may be helpful in this regard, since it provides more information of the chemical state and environment of measured elements.

The discussed analyses have so far focussed on the inorganic part of the nanocrystals. While this part accounts for a large portion of the interesting properties of NCs, the organic capping ligands play an important role as well. The results discussed in Appendix 4 show that mixing with ligating molecules has an influence on the assembly behaviour of the NCs. However, the actual ligands which cap the NCs are not determined. To this end, fourier-transform infra-red (FTIR) spectroscopy may be interesting. A number of attempts were made to analyse the NCs with this technique. However, the NC solvent, toluene, proofed a problem: recorded FTIR spectra were dominated by peaks attributed to toluene, even after drying and redispersion in tetrachloro ethylene (TCE). Future FTIR spectroscopic studies should thus find a way of removing toluene from the sample, possible by placing the sample under mild vacuum (to prevent evaporation of ligands).

Cation exchange in nanocrystals with other morphologies

The results presented in this thesis only include reactions with bifrustum and bipyramid $Cu_{2-x}S$ nanocrystals, and some preliminary experiments with small sphere-like $Cu_{2-x}S$ nanocrystals (Appendix 4). However, $Cu_{2-x}S$ nanocrystals with a wide range of morphologies can be synthesized. Attempts were made to perform cation exchange reactions on $Cu_{2-x}S$ small spheres, nanoplatelets, nanosheets and larger bifrustums. These attempts were largely unsuccessful: in the case of the nanoplatelets and nanosheets, initial attempts resulted in the formation of smaller, bifrustum-like NCs (Appendix Figure 11). In the case of the larger bifrustums, no changes were observed. Reacting small $Cu_{2-x}S$ NCs with $GaCl_3$ at elevated temperatures yields larger NCs, which show interesting stacking behaviour (Appendix Figure 12).

One of the attractive properties of the cation exchange procedure, is that the product NCs inherit the morphology and crystal structure of the parent particles. It would thus be unfortunate if the procedure would be limited to certain NC morphologies, since that would, in part, undo the attractiveness of the procedure. A better understanding of the influence of NC shape on cation exchange reactions is therefore necessary. Further research could expand on the present work by applying the presented procedures to differently shaped nanocrystals.

Sequential exchanges to $CuIn_xGa_{1-x}S$ nanocrystals

During this research, no luminescence from $CuGaS_2$ nanocrystals was observed. However, $CuInS_2$ nanocrystals obtained by cation exchange readily luminesce. $CuIn_xGa_{1-x}S_2$ (CIGS) is also expected to luminesce. Cation exchange may be used to obtain all sorts of novel CIGS (containing) nanocrystals. For example, the bipyramids discussed above appear to consist partially of low-chalcocite $Cu_{2-x}S$, and partially of wurtzite CGS. Early quenching of the reaction may result in particles wherein only the tips are CGS. A next step could be cation exchange with In^{3+}, possibly resulting in $Cu_{2-x}S$/CIGS center/tips bipyramid nanocrystals. If the size of the CIGS region within these NCs is small enough, quantum confinement effects may be induced, resulting in interesting optical properties. Such sequential cation exchanges are of course not limited to bipyramid-shaped nanocrystals; sequential cation exchanges in other nanocrystals may also result in particles with interesting properties.

Some experiments were performed on small CIS nanocrystals, in an attempt to produce luminescent CIGS particles, by reacting with $GaCl_3$-TOP. However, the product particles showed very little change in their emission spectra. Use of other precursors (such as $GaCl_3$-TPP or $GaCl_3$-DPP) may proof more successful. Some preliminary experiments were performed to this end, with no observed luminescence. However, the use of milder reaction conditions and additional ligands may make cation exchange possible in these particles, since the reaction rate is assumed to be large, due to the small particle size and relatively large surface/volume ratio.

Extension to other elements

Part of the present research was the adaption of an existing cation exchange procedure (for the conversion of $Cu_{2-x}S$ into $CuInS_2$) for different elements. Initial experiments using $AlCl_3$-TOP, $SbCl_3$-TOP and $BiCl_3$-TOP failed. However, the lessons learned in this project may proof helpful for cation exchange reactions of Cu^+ in $Cu_{2-x}S$ for other elements, which may yield nanocrystals with novel opto-electronic properties.

7. Acknowledgements

First of all, I would like to thank Celso de Mello Donegá and Ward van der Stam. Your supervision has been a great help during this project, and I have learned a lot from you. Celso, I enjoyed the lengthy discussions and brainstorming sessions. Your advice, be it related to my project, my internship or something else, was very helpful. Ward, you have taught me a lot about the synthesis of nanocrystals and their characterization. I really enjoyed my project, which was in part because you let me make it my own. I am grateful for the opportunities you both have given me. Being able to go along with Ward for the beam trip at the ESRF was a unique experience. I had followed courses dealing with synchrotrons, but being able to visit one, and to do actual experiments, is something completely different. Apart from being scientifically interesting, the trip was also very bonding. I have fond memories of shared shifts with Freddy Rabouw and Robin Geitenbeek, as well as the time we spent together with the whole group.

The work shown in this thesis would not have been possible without the help of a number of people. Hans Ligthart was always helpful whenever a glovebox was high on oxygen, when a heating mantle decided to stop heating or when other technical difficulties manifested themselves. Hans Meeldijk helped with EDX analysis, as well as measuring elemental mapping on the new Talos microscope. I think each time we went to you to do measurements, we returned with a much better understanding of our systems. Furthermore, I think you were the first to recognize the true morphology of the ‘hollow’ particles, although “ingetrapte voetbal” may not be a very *catchy* description. Stephan Zevenhuizen has helped by performing TEM measurements, and administrating the computers at CMI. I would like to thank Gang Wang for his help with the XRD analysis. For some of the characterization, we had help from researchers at the University of Antwerp: Naomi Winckelmans performed elemental mapping. Mert Kurttepeli did so as well, along with HRTEM and tomography measurements, the latter of which were invaluable for the study of the hollow particles. Regarding my failed attempts to measure usable FTIR spectra, I would like to thank Kees van Walree for letting us use his FTIR apparatus, Maro for helping me with FTIR measurements, and Joep for letting me use his KBr-sample holder. I would like to thank Jip for all her support during my thesis, especially during the last more demanding period. It was a great help knowing I could count on your support.

The people at CMI are the ones who made my time there enjoyable. The people I saw most were perhaps my masterroom-roommates. Stephan, Christiaan, Franscesca, John, Naud, Corneel, Bas and Daniel jr., thank you for the nice and fun times, as well as your (un)solicited advice. Of course, we also had very kind neighbours in the other master room: Adriaan, Riande, Marieke, Tim, Marc, Thomas, thank you for the fun times. I would also like to thank all other students, researchers, and staff members. Thank you all for the fun, interesting and educational time!

8. References

[1] P. V. Kamat, “Quantum Dot Solar Cells. Semiconductor Nanocrystals as Light Harvesters,” *J. Phys. Chem. C*, vol. 112, no. 48, pp. 18737–18753, 2008.

[2] X. Dai, Z. Zhang, Y. Jin, Y. Niu, H. Cao, X. Liang, L. Chen, J. Wang, and X. Peng, “Solution-processed, high-performance light-emitting diodes based on quantum dots,” *Nature*, vol. 515, no. 7525, pp. 96–99, 2014.

[3] G. Hong, J. T. Robinson, Y. Zhang, S. Diao, A. L. Antaris, Q. Wang, and H. Dai, “In vivo fluorescence imaging with Ag2S quantum dots in the second near-infrared region,” *Angew. Chemie - Int. Ed.*, vol. 51, no. 39, pp. 9818–9821, 2012.

[4] H. M. Haverinen, R. a. Myllylä, and G. E. Jabbour, “Inkjet printing of light emitting quantum dots,” *Appl. Phys. Lett.*, vol. 94, pp. 86–89, 2009.

[5] C. de Mello Donegá, “Synthesis and properties of colloidal heteronanocrystals.,” *Chem. Soc. Rev.*, vol. 40, no. 3, pp. 1512–46, 2011.

[6] C. B. Murray, D. J. Norris, and M. G. Bawendi, “Synthesis and characterization of nearly monodisperse CdE (E = S, Se, Te) semiconductor nanocrystallites,” *J. Am. Chem. Soc.*, vol. 115, no. 19, pp. 8706–8715, 1993.

[7] X. Peng, L. Manna, W. Yang, J. Wickham, E. Scher, A. Kadavanich, and A. P. Alivisatos, “Shape control of CdSe nanocrystals,” *Nature*, vol. 404, pp. 59–61, 2000.

[8] Z. A. Peng and X. Peng, “Mechanisms of the shape evolution of CdSe nanocrystals,” *J. Am. Chem. Soc.*, vol. 123, no. 7, pp. 1389–1395, 2001.

[9] Li. Qu and X. Peng, “Control of photoluminescence properties of CdSe nanocrytals in growth,” *J. Am. Chem. Soc.*, vol. 124, no. 9, pp. 2016–2018, 2016.

[10] W. van der Stam, A. C. Berends, and C. de Mello Donegá, “Prospects of Colloidal Copper Chalcogenide Nanocrystals,” *ChemPhysChem*, DOI 10.1002/cphc.201500976, 2016.

[11] B. J. Beberwyck, Y. Surendranath, and A. P. Alivisatos, “Cation Exchange: A Versatile Tool for Nanomaterials Synthesis,” *J. Phys. Chem. C*, vol. 117, no. 39, pp. 19759–19770, 2013.

[12] D. H. Son, S. M. Hughes, Y. Yin, and A. P. Alivisatos, “Cation exchange reactions in ionic nanocrystals.,” *Science*, vol. 306, no. 5698, pp. 1009–1012, 2004.

[13] V. A. Vlaskin, C. J. Barrows, C. S. Erickson, and D. R. Gamelin, "Nanocrystal Diffusion Doping," *J. Am. Chem. Soc.*, vol. 135, pp. 14380–14389, 2013.

[14] W. van der Stam, E. Bladt, F. T. Rabouw, S. Bals, and C. de Mello Donega, "Near-Infrared Emitting CuInSe 2 /CuInS 2 Dot Core/Rod Shell Heteronanorods by Sequential Cation Exchange," *ACS Nano*, vol. 26, pp. 3002–3008, 2015.

[15] Y.-H. A. Wang, X. Zhang, N. Bao, B. Lin, and A. Gupta, "Synthesis of Shape-Controlled Monodisperse Wurtzite CuIn x Ga1–x S2 Semiconductor Nanocrystals with Tunable Band Gap," *J. Am. Chem. Soc.*, vol. 133, pp. 11072–11075, 2011.

[16] E. Dilena, Y. Xie, R. Brescia, M. Prato, L. Maserati, R. Krahne, A. Paolella, G. Bertoni, M. Povia, I. Moreels, and L. Manna, "CuInxGa1-xS2 Nanocrystals with Tunable Composition and Band Gap Synthesized via a Phosphine-Free and Scalable Procedure," *Chem. Mater.*, vol. 25, pp. 3180–3187, 2013.

[17] T. A. Kandiel, D. H. Anjum, P. Sautet, T. Le Bahers, and K. Takanabe, "Electronic structure and photocatalytic activity of wurtzite Cu–Ga–S nanocrystals and their Zn substitution," *J. Mater. Chem. A*, vol. 3, pp. 8896–8904, 2015.

[18] Q. Zhou, S.-Z. Kang, L. Xiangqing, L. Wang, L. Qin, and J. Mu, "One-pot hydrothermal preparation of wurtzite CuGaS2 and its application as a photoluminescent probe for trace detection of l-noradrenaline," *Colloids Surfaces A Physicochem. Eng. Asp.*, vol. 465, pp. 124–129, Jan. 2015.

[19] R. Koole, E. Groeneveld, D. Vanmaekelbergh, A. Meijerink, and C. de Mello Donegá, "Size Effects on Semiconductor Nanoparticles," in *Nanoparticles: Workhorses of Nanoscience*, 1st ed., C. de Mello Donegá, Ed. Berlin: Springer-Verlag, 2014, pp. 13–51.

[20] E. Groeneveld, "Synthesis and optical spectroscopy of (hetero)-nanocrystals," PhD Thesis, Utrecht University, 2012.

[21] S. V. Gaponenko, *Introduction to Nanophotonics*. Cambridge: Cambridge University Press, 2010.

[22] E. Groeneveld and C. de Mello Donegá, "The Challenge of Colloidal Nanoparticle Synthesis," in *Nanoparticles: Workhorses of Nanoscience*, 1st ed., C. de Mello Donegá, Ed. Berlin: Springer-Verlag, 2014, pp. 145–189.

[23] J. P. den Breejen, P. B. Radstake, G. L. Bezemer, J. H. Bitter, V. Frøseth, A. Holmen, and K. . de Jong, "On the Origin of the Cobalt Particle Size Effects in Fischer-Tropsch Catalysis," *J. Am. Chem. Soc.*, vol. 131, pp. 7197–7203, 2009.

[24] L. Manna and S. Kudera, “Mechanisms underlying the growth of inorganic nanoparticles in the liquid phase.,” in *Advanced Wet-Chemical Synthetic Approaches to Inorganic Nanostructures*, Transworld., Kerala, 2008, pp. 1–53.

[25] L. Carbone and P. D. Cozzoli, “Colloidal heterostructured nanocrystals: Synthesis and growth mechanisms,” *Nano Today*, vol. 5, no. 5, pp. 449–493, 2010.

[26] E. Groeneveld, L. Witteman, M. Lefferts, X. Ke, S. Bals, and G. Van Tendeloo, “Tailoring ZnSe-CdSe Colloidal Quantum Dots via Cation Exchange: From Core/Shell to Alloy Nanocrystals,” *ACS Nano*, vol. 7, no. 9, pp. 7913–7930, 2013.

[27] R. Pearson, “Absolute electronegativity and hardness: application to inorganic chemistry,” *Inorg. Chem.*, vol. 27, no. 4, pp. 734–740, 1988.

[28] P. H. C. Camargo, Y. H. Lee, U. Jeong, Z. Zou, and Y. Xia, “Cation exchange: A simple and versatile route to inorganic colloidal spheres with the same size but different compositions and properties,” *Langmuir*, vol. 23, no. 6, pp. 2985–2992, 2007.

[29] H. Li, M. Zanella, A. Genovese, M. Povia, A. Falqui, C. Giannini, and L. Manna, “Sequential cation exchange in nanocrystals: preservation of crystal phase and formation of metastable phases.,” *Nano Lett.*, vol. 11, no. 11, pp. 4964–70, 2011.

[30] L. Mu, F. Wang, B. Sadtler, R. a. Loomis, and W. E. Buhro, “Influence of the Nanoscale Kirkendall Effect on the Morphology of Copper Indium Disulfide Nanoplatelets Synthesized by Ion Exchange,” *ACS Nano*, vol. 9, no. 7, pp. 7419–7428, 2015.

[31] D.-H. Ha, A. H. Caldwell, M. J. Ward, S. Honrao, K. Mathew, R. Hovden, M. K. A. Koker, D. A. Muller, R. G. Hennig, and R. D. Robinson, “Solid–Solid Phase Transformations Induced through Cation Exchange and Strain in 2D Heterostructured Copper Sulfide Nanocrystals,” *Nano Lett.*, vol. 14, pp. 7090–7099, 2014.

[32] S. E. Wark, C.-H. Hsia, and H. S. Dong, “Effects of ion solvation and volume change of reaction on the equilibrium and morphology in cation-exchange reaction of nanocrystals,” *J. Am. Chem. Soc.*, vol. 130, pp. 9550–9555, 2008.

[33] W. van der Stam, A. C. Berends, F. T. Rabouw, T. Willhammar, X. Ke, J. D. Meeldijk, S. Bals, and C. de Mello Donega, “Luminescent CuInS 2 Quantum Dots by Partial Cation Exchange in Cu2-xS Nanocrystals,” *Chem. Mater.*, vol. 27, no. 2, pp. 621–628, Jan. 2014.

[34] S. Kasap and P. Capper, *Springer Handbook of Electronic and Photonic Materials*. Springer US, 2007.

[35] A. J. Nozik, “Quantum dot solar cells,” *Phys. E*, vol. 14, pp. 115–120, 2002.

[36] Samsung, “65" Curved 4K SUHD,” 2016. [Online]. Available: http://www.samsung.com/us/video/tvs/UN65JS9500FXZA. [Accessed: 31-Jan-2016].

[37] M. G. Debije and P. P. C. Verbunt, “Thirty years of luminescent solar concentrator research: Solar energy for the built environment,” *Adv. Energy Mater.*, vol. 2, pp. 12–35, 2012.

[38] M. Bruchez, M. Moronne, P. Gin, S. Weiss, and A. P. Alivisatos, “Semiconductor nanocrystals as fluorescent biological labels.,” *Science*, vol. 281, no. 5385, pp. 2013–2016, 1998.

[39] J. M. Klostranec and W. C. W. Chan, “Quantum dots in biological and biomedical research: Recent progress and present challenges,” *Adv. Mater.*, vol. 18, no. 15, pp. 1953–1964, 2006.

[40] W. van der Stam, A. P. Gantapara, Q. A. Akkerman, G. Soligno, J. D. Meeldijk, R. van Roij, M. Dijkstra, and C. de Mello Donegá, “Self-Assembly of Colloidal Hexagonal Bipyramid- and Bifrustum-Shaped ZnS Nanocrystals into Two-Dimensional Superstructures.,” *Nano Lett.*, vol. 14, no. 2, pp. 1032–7, 2014.

[41] M. Klinger and A. Jäger, “Crystallographic Tool Box (CrysTBox): automated tools for transmission electron microscopists and crystallographers,” *J. Appl. Crystallogr.*, vol. 48(6), 2015.

[42] C. Gammer, C. Mangler, C. Rentenberger, and H. P. Karnthaler, “Quantitative local profile analysis of nanomaterials by electron diffraction,” *Scr. Mater.*, vol. 63, no. 3, pp. 312–315, 2010.

[43] K. Momma and F. Izumi, “*VESTA 3* for three-dimensional visualization of crystal, volumetric and morphology data,” *J. Appl. Crystallogr.*, vol. 44, no. 6, pp. 1272–1276, 2011.

[44] F. Izumi and K. Momma, “Three-dimensional visualization in powder diffraction,” *Solid State Phenom.*, vol. 130, pp. 15–20, 2007.

[45] H. T. Evans, “Crystal Structure of Low Chalcocite,” *Nat. Phys. Sci.*, vol. 232, pp. 69–70, 1971.

[46] N. Xiao, L. Zhu, K. Wang, Q. Dai, Y. Wang, S. Li, Y. Sui, Y. Ma, J. Liu, B. Liu, G. Zou, and B. Zou, “Synthesis and high-pressure transformation of metastable wurtzite-structured CuGaS2 nanocrystals.,” *Nanoscale*, vol. 4, no. 23, pp. 7443–7, 2012.

[47] T. Ruberu, H. Albright, and B. Callis, “Molecular Control of the Nanoscale: Effect of Phosphine–Chalcogenide Reactivity on CdS–CdSe Nanocrystal Composition and Morphology,” *ACS Nano*, no. 6, pp. 5348–5359, 2012.

[48] S. Nogai and H. Schmidbaur, “Dichlorogallane (HGaCl2)2: Its Molecular Structure and Synthetic Potential,” *Inorg. Chem.*, vol. 41, no. 18, pp. 4770–4774, 2002.

[49] F. Cheng, H. L. Codgbrook, A. L. Hector, W. Levason, G. Reid, M. Webster, and W. Zhang, “Gallium(III) halide complexes with phosphines, arsines and phosphine oxides – a comparative study,” *Polyhedron*, vol. 26, no. 15, pp. 4147–4155, 2007.

[50] M. P. Pardo, M. Guittard, A. Chilouet, and A. Tomas, “Diagramme de phases gallium-soufre et études structurales des phases solides,” *J. Solid State Chem.*, vol. 102, pp. 423–433, 1993.

[51] H. J. Fan, U. Gösele, and M. Zacharias, “Formation of Nanotubes and Hollow Nanoparticles Based on Kirkendall and Diffusion Processes: A Review,” *Small*, vol. 3, no. 10, pp. 1660–1671, 2007.

[52] A. Cabot, M. Ibánez, P. Guardia, and A. P. Alivisatos, “Reaction regimes on the synthesis of hollow particles by the Kirkendall effect,” *J. Am. Chem. Soc.*, pp. 11326–11328, 2009.

[53] R. W. G. Wyckoff, *Crystal Structures*, 2nd ed. New York: Interscience Publishers, 1963.

[54] A. A. Silva, R. A. Reis, and M. L. L. Paredes, “Density and Viscosity of Decalin, Cyclohexane, and Toluene Binary Mixtures at (283.15, 293.15, 303.15, 313.15 , and 323.15) K,” *J. Chem. Eng. Data*, vol. 54, no. 7, pp. 2067–2072, 2009.

Appendix

Appendix 1*:* Derivation of the sedimentation rate of colloidal nanocrystals

We can use Stokes' law to describe the frictional force on nanocrystals (NCs), assuming spherical particles and flow at small Reynolds numbers. The former is a crude approximation. In the case of NCs, the latter applies well. Stokes' law states:

$$F_d = 6\pi\eta a u \tag{A1}$$

With η the viscosity of the liquid, a the radius of the NC and u the velocity. The force of gravity is:

$$F_g = \Delta m g \tag{A2}$$

With Δm the reduced mass of the NC and g the gravitational acceleration. We use the reduced mass of the NC to account for buoyancy. Expression A2 can be rewritten to:

$$F_g = V_{NC}(\rho_{NC} - \rho_l)g = \tfrac{4}{3}\pi a^3(\rho_{NC} - \rho_l)g \tag{A3}$$

With V_{NC} the volume of the NC, ρ_{NC} the density of the NC and ρ_l the density of the liquid in which the NCs are dispersed. Under steady-state conditions, we can assume a net force of zero; the force of friction and the force of gravity cancel each other out:

$$F_d = -F_g = 6\pi\eta a u = -\tfrac{4}{3}\pi a^3(\rho_{NC} - \rho_l)g \tag{A4}$$

Solving for the velocity u yields an expression for the sedimentation rate of the dispersed NCs:

$$u = -\frac{2a^2(\rho_{NC}-\rho_l)g}{9\eta} \tag{A5}$$

This expression shows that the sedimentation rate has a quadratic dependence on the NC radius. The minus sign indicates that the direction of sedimentation is downward. The obtained expression is a rather crude model. For example, it does not take into account the layer of organic ligands on the NC surface (this layer would substantially increase the hydrodynamic radius of the NCs, but is not expected to contribute much to the NC mass. Actual sedimentation rates may thus be significantly lower than estimated using Equation A5.)

Using values which are applicable to CdSe NCs dispersed in toluene ($\rho_{NC} = 5.65 \cdot 10^6$ g m^{-3}, bulk value[53], $\rho_l = 0.867 \cdot 10^6$ g m^{-3} [54], $\eta = 0.596$ g cm^{-1} s^{-1} [54]) we find for a NC with a radius of 2.0 nm:

$$u_{CdSe,2nm} = -\frac{2(2 \cdot 10^{-9}\,\mathrm{m})^2(5.96 \cdot 10^6\,\mathrm{gm^{-3}} - 0.867\,\mathrm{gm^{-3}}) \cdot 9.81\mathrm{ms^{-2}}}{9 \cdot 0.590 \cdot 10^2\,\mathrm{gm^{-1}s^{-1}}} = -7.0 \cdot 10^{-13}\,\mathrm{m/s}$$
$$= -2.5\,\mathrm{nm/h}$$

Appendix 2: Derivation of the surface/volume ratio for spherical particles

The surface *S* of a sphere is a function of its radius:

$$S = 4\pi r^2 \tag{A6}$$

The volume *V* is so as well:

$$V = (4/3)\pi r^3 \tag{A7}$$

The surface/volume ratio is thus given by:

$$S/V = (1/3)r^{-1} \tag{A8}$$

Appendix 3: Derivation of the critical nucleus radius

The total Gibbs free energy difference associated with nucleus formation is:

$$\Delta G_{tot} = \frac{4}{3}\pi r^3 \rho \Delta\mu + 4\pi r^2 \gamma \tag{A9}$$

Derivation with respect to r yields:

$$\frac{d\Delta G_{tot}}{dr} = 3\pi r^2 \rho \Delta\mu + 8\pi r \gamma \tag{A10}$$

Equating the derivative to zero and solving for *r* yields the critical nucleus radius:

$$r_c = -\frac{2\gamma}{\rho \Delta\mu} \tag{A11}$$

Appendix 4: Miscellaneous experiments

Some of the performed experiments did not yield clear results, either because the results were ambiguous, or because further analysis is necessary. Nonetheless, results from these experiments may be interesting to discuss. Thus, some of these experiments will be discussed below.

Self-assembly behaviour of $Cu_{2-x}S$ bifrustum nanocrystals

$Cu_{2-x}S$ bifrustum NCs tend to form regular three-dimensional (3D) supercrystals (Figure 16a). However, after reacting with $GaCl_3$-TOP, the particles no longer form regular 3D structures. Instead, they tend to assemble in two-dimensional (2D) monolayers (Figure 26a). Since this reaction coincides with the incorporation of only a few percent of Ga into these NCs, the change in assembly behaviour is likely to be caused by a change in the surface of the NC (since only a very small portion of the interior of the NC is changed). An important component of the NC surface is the layer of organic capping ligands. Without these ligands, the particles will cluster together. These ligands thus play a role in the clustering behaviour of NCs. Therefore, the influence of the type of organic capping ligands on the self-assembly behaviour of bifrustum $Cu_{2-x}S$ NCs was studied.

These experiments were performed by mixing the particles with oleic acid (OA) or dodecane thiol (DDT). In this way, a ligand exchange of the original ligands for these molecules was attempted. Initial NC samples used for these procedures were Cu_2S:Ga NCs, obtained by reacting $Cu_{2-x}S$ NCs with $GaCl_3$-TOP at 100°C overnight, and $Cu_{2-x}S$-THF NCs, obtained by dispersing the $Cu_{2-x}S$ NCs in tetrahydrofuran (THF) at 50°C overnight. These particle types were chosen, because their stacking behaviour differs substantially from the parent $Cu_{2-x}S$ bifrustum NCs: Cu_2S:Ga NCs tend to assemble into 2D monolayers (Figure 26a) and $Cu_{2-x}S$-THF NCs stack in 3D, but in an irregular manner (Figure 26d). OA and DDT were used as ligands, because these are used in the synthesis of the $Cu_{2-x}S$ bifrustum nanocrystals. Thus, it is expected that these coat the parent bifrustum NCs. Ligand exchange, to add these ligands to the Cu_2S:Ga and $Cu_{2-x}S$-THF NCs may restore the original assembly behaviour.

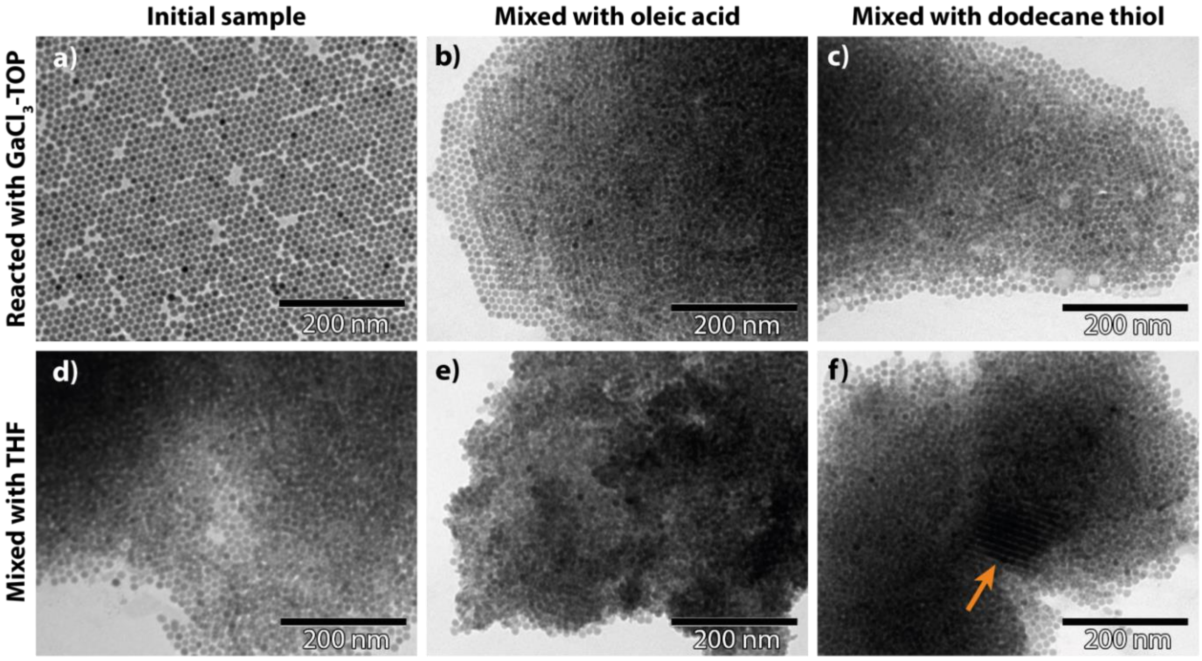

Figure 26. TEM micrographs of (a) Cu_2S:Ga bifrustum nanocrystals, obtained by reacting $Cu_{2-x}S$ nanocrystals with $GaCl_3$-TOP at 100°C, overnight; Cu_2S:Ga bifrustum nanocrystals, mixed for 24h at 30°C with (b) oleic acid, (c) dodecane and (d) $Cu_{2-x}S$ bifrustum nanocrystals, mixed with THF at 50°C, overnight ($Cu_{2-x}S$-THF); $Cu_{2-x}S$-THF nanocrystals mixed for 6h at 30°C with (e) oleic acid, (f) dodecane thiol. Orange arrow indicates an area where nanocrystals form an ordered three-dimensional assembly.

After mixing Cu_2S:Ga NCs with OA, the particles form irregular 3D assemblies, instead of regular 2D monolayers (Figure 26b). Mixing the same NCs with DDT has the same result, although some of the particles are affected by the treatment: larger, brigher particles can be seen in the TEM micrograph (Figure 26c). The $Cu_{2-x}S$-THF particles are also affected by mixing with either OA or DDT. After treatment with the former, the particles form agglomorates in which the particles appear to be closer to each other than before the treatment (Figure 26e). After treatment with DDT, agglomorates appear similar to before the treatment. However, in some regions the particles again form regular 3D assemblies (Figure 26f).

These results show that mixing with OA or DDT can influence the stacking behaviour of bifrustum NCs. This suggests that the ligands which cap the NC surface play an important role in the self-assembly behaviour of the NCs, as was presumed above.

Shape conservation during cation exchange of Cu^+ for Ga^{3+}

Although the cation exchange reaction by reaction of $Cu_{2-x}S$ nanocrystals with $GaCl_3$-DPP yields particles which have the CGS composition, the particles have sintered (Figure 12). This makes these particles unsuitable for further applications. It is therefore interesting to try to prevent this sintering. Because it was thought the cation exchange reaction would be reasonably slow, the reaction was performed for only 5 minutes (instead of 60 minutes), in an attempt to prevent sintering. The same was done in the reaction with $GaCl_3$-TOP, to study if the self-assembly behaviour of these particles would be altered after such a short reaction time.

Particles obtained after reaction with $GaCl_3$-TOP for 5 minutes form two-dimensional monolayers (Figure 27a). After reacting with $GaCl_3$-DPP for 5 minutes, the particles have already sintered (Figure 27b). These results indicate that the surface of the NC is already affected after a reaction time of 5 minutes, and that this time is not short enough to prevent sintering.

To slow down the reaction and provide more steric stabilization for the NCs, CE reactions were performed at lower temperatures, with an additional ligand (oleyl amine, OLAM). After reacting with $GaCl_3$-DPP, in the presence of OLAM at 50°C, the particles have not sintered, and have maintained their shape reasonably well (Figure 28a). SAED analysis indicates these particles have the wurtzite $CuGaS_2$ crystal structure (Figure 28d), indicating the cation exchange reaction may have been successful.

After reaction with $GaCl_3$-TPP under the same reaction conditions, the particles still exhibit the low-chalcocite $Cu_{2-x}S$ crystal structure (Figure 28e). In TEM micrographs, the particles appear unchanged. However, a large, gel-like substance is present, which may be unreacted precursor material (Figure 28b). Reacting these particles at a slightly elevated temperature, 75°C, results in non-sintered particles, some of which show intraparticle contrast (Figure 28c). The SAED pattern of this sample cannot be directly ascribed to either low-chalcocite $Cu_{2-x}S$ or wurtzite $CuGaS_2$: it shows similarities to both patterns (Figure 28f). It is thus possible that the cation exchange in these particles has yielded heteronanostructured nanocrystals.

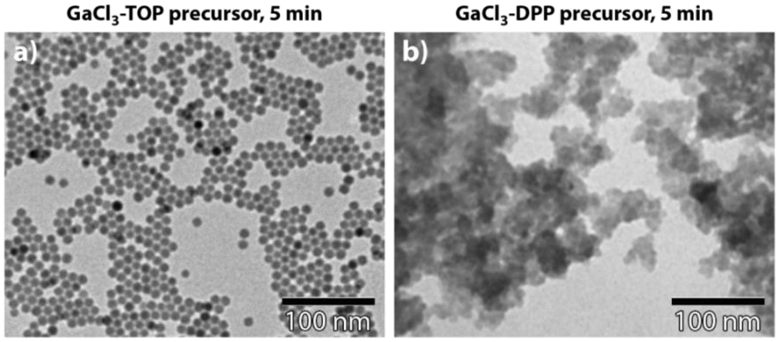

Figure 27. TEM micrographs of (a) $Cu_{2-x}S$ nanocrystals after reaction with $GaCl_3$-TOP at 100 °C, for 5 minutes; (b) $(Cu,Ga)S_2$ nanocrystals after reaction with $GaCl_3$-DPP at 100 °C for 5 minutes.

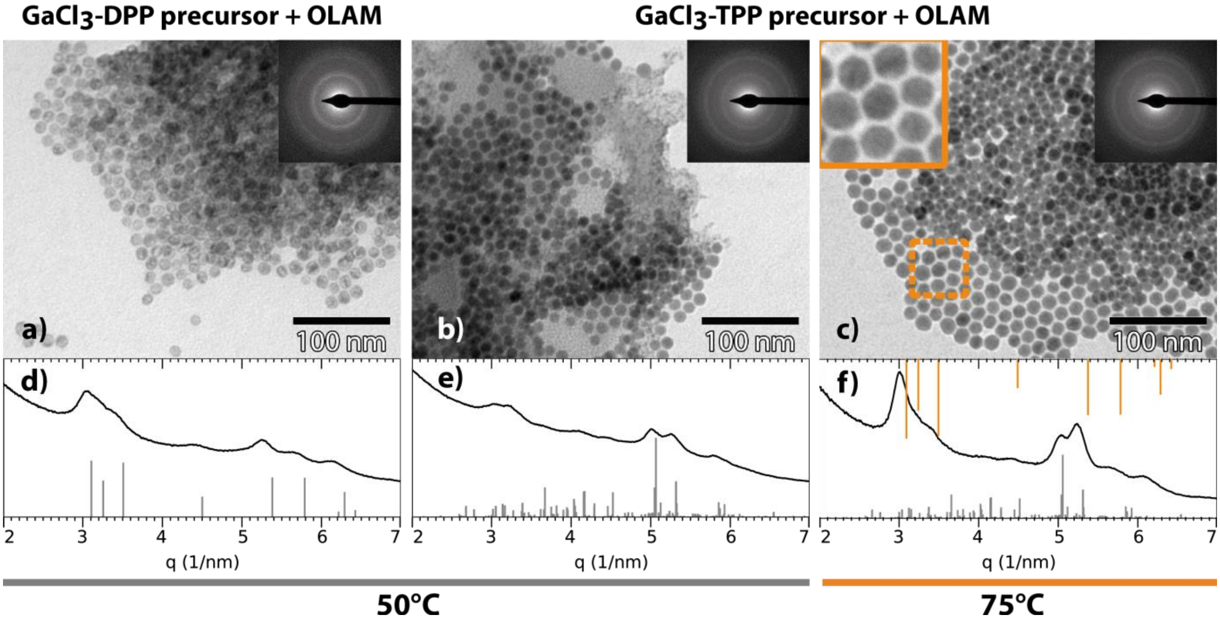

Figure 28. TEM micrographs of (a) $CuGaS_2$ nanocrystals, reacted with $GaCl_3$-DPP, at 50°C, for 60 minutes; (b) $Cu_{2-x}S$ nanocrystals, reacted with $GaCl_3$-TPP, at 50°C, for 60 minutes; (c) $Cu_{2-x}S/CuGaS_2$ nanocrystals, reacted with $GaCl_3$-TPP at 75°C, for 60 minutes. Top-left inset is an enlargement of the highlighted area. Top-right insets are selected-area electron diffractograms of the depicted samples. These were rotationally averaged (e-g). Reference bars are calculated patterns based on (a, orange bar in f) the crystal structure described in [46]**; (e, grey bar in f) the crystal structure described in** [45]**.**

Unfortunately, it was not possible to determine the elemental composition of these NCs, due to time limitations. However, the SAED pattern of the sample reacted with $GaCl_3$-DPP at 50°C indicates that the cation exchange reaction may have been succesful, without sintering the particles. This shows that the addition of ligands to the reaction mixture, and reacting at a lower temperature, may help to prevent sintering in this cation exchange reaction.

Luminescent $CuIn_xGa_{1-x}S_2$ nanocrystals via cation exchange

The lessons learned from performing CE reactions on relatively large $Cu_{2-x}S$ NCs may be used to alter the composition of smaller $Cu_{2-x}S$ NCs. If these reactions are successful, the resulting CGS NCs may show luminescence. Unfortunately, no luminescence was observed in small $Cu_{2-x}S$ NCs reacted with Ga cation exchange precursors. Thus, another approach may be more fruitful: cation exchange in CIS NCs to $CuIn_xGa_{1-x}S_2$ (CIGS) NCs. It was shown previously that CIGS with a wide range of compositions (x ranging from 0 to 1) could be produced.[15] Succesful exchange should accompanied by a substantial redshift,[15] making it relatively easy to study this reaction using photoluminscence emission spectroscopy.

Cation exchange in $Cu_{2-x}S$ bifrustums using $GaCl_3$-TOP as precursor exchanges only a few percent of Cu^+ for Ga^{3+}. However, smaller NCs consist of less atoms than larger ones. Thus, a comparable number of exchanged cations results in a larger overall percentage of exchanged cations. Thus it was tried to convert small CIS NCs (obtained via CE from small $Cu_{2-x}S$ NCs) into CIGS NCs using $GaCl_3$-TOP. These reactions were performed on four different sizes of CIS NCs, to also study any influence of NC size.

Unfortunately, in all four cases, the CE reaction resulted in samples which showed only a minor blueshift in the emission spectrum, with little change in the excitation spectrum (Figure 29). This excludes that the CE reaction was successful, since a much larger blueshift is to be expected. However, there are multiple explanations for this small blueshift: (i) the particles may have become smaller during the reaction, resulting in a larger degree of quantum confinement and thus a larger band gap, (ii) only a very small number of In^{3+} may have been replaced by Ga^{3+} or (iii) In^{3+} was only replaced by Ga^{3+} in the outer part of the NC; the resulting CIS/CGS core/shell NC may have a luminescent core (which is smaller than the initial NC size, see (i)), with a non-luminescent shell.

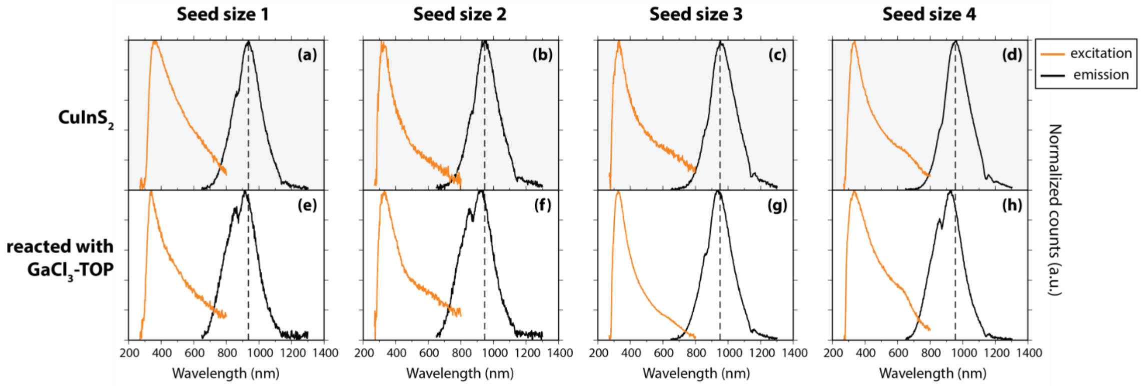

Figure 29. Excitation and emission spectra of (a-d) $CuInS_2$ nanocrystals obtained by reaction of $Cu_{2-x}S$ nanocrystals with $InCl_3$-TOP, (e-h) the $CuInS_2$ nanocrystals after reaction with $GaCl_3$-TOP. Four different $Cu_{2-x}S$ nanocrystal sizes obtained by different synthesis durations: (a,e) 120 minutes, (b,f) 150 minutes, (c,g) 180 minutes and (d,h) 215 minutes.

Appendix 5: Supporting and additional figures

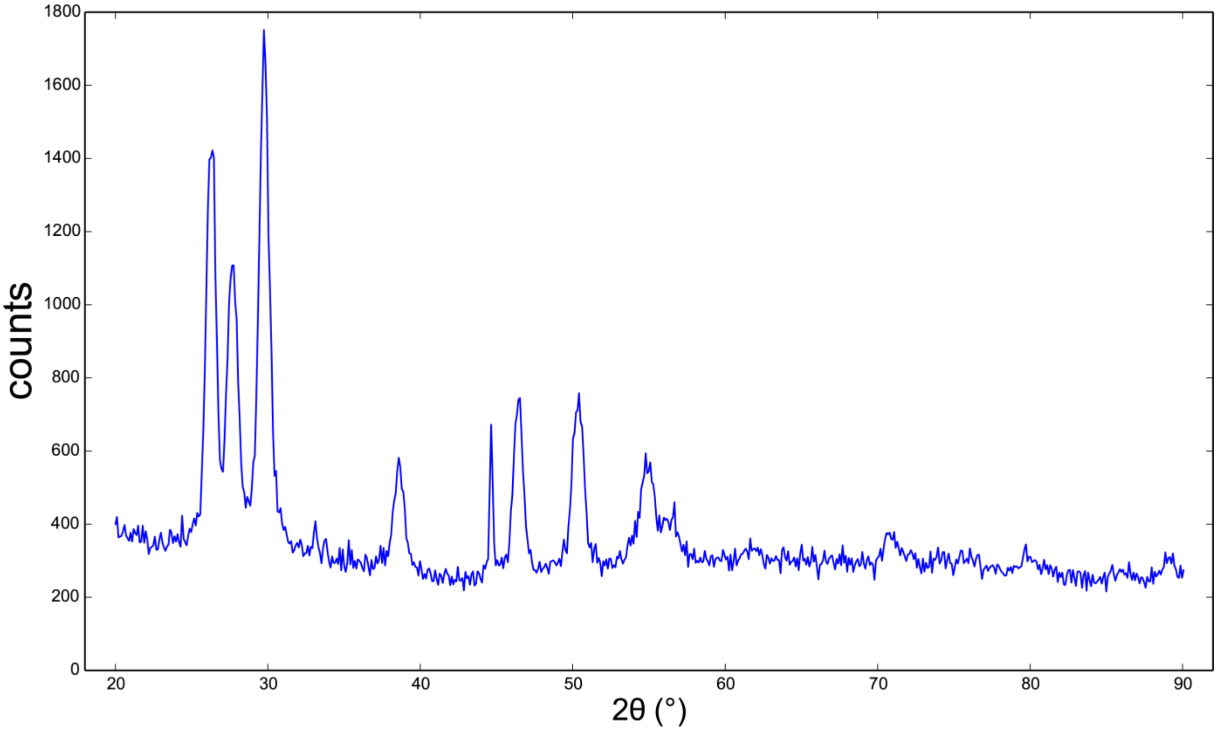

Appendix Figure 1. XRD pattern of $CuInS_2$ nanocrystals, obtained by reacting $Cu_{2-x}S$ bifrus*t*um parent nanocrystals with $InCl_3$-TOP at 100°C, overnight.

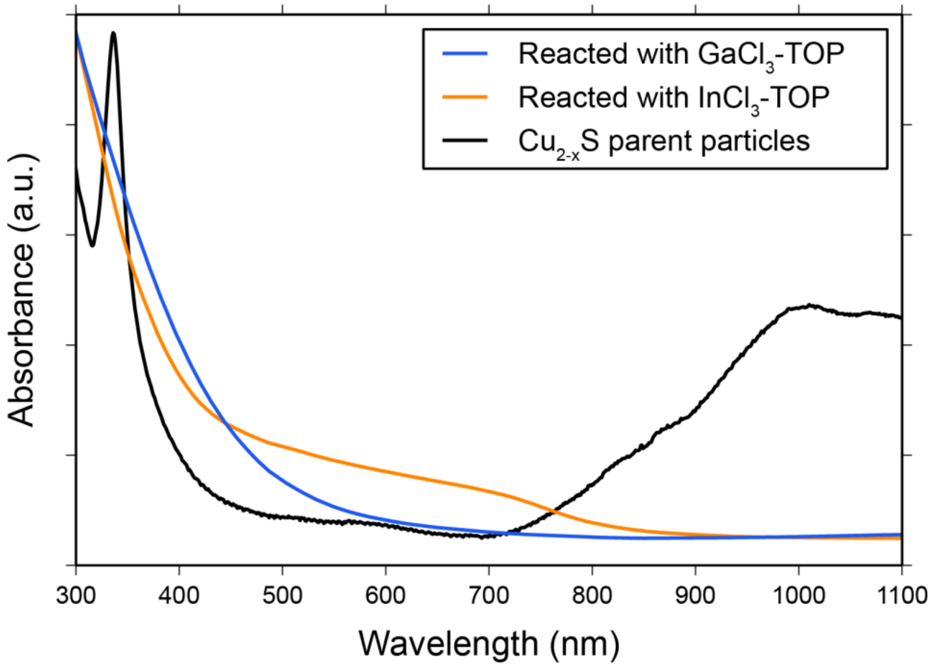

Appendix Figure 2. Absorption spectra of (bottom, black) the parent $Cu_{2-x}S$ bifrustum nanocrystals; (middle, orange) $CuInS_2$ nanocrystals, obtained by reaction of the parent $Cu_{2-x}S$ nanocrystals with $InCl_3$-TOP at 100°C, overnight; (top, blue) Cu_2S:Ga nanocrystals, obtained by reaction of the parent $Cu_{2-x}S$ nanocrystals with $GaCl_3$-TOP, at 100°C, overnight.

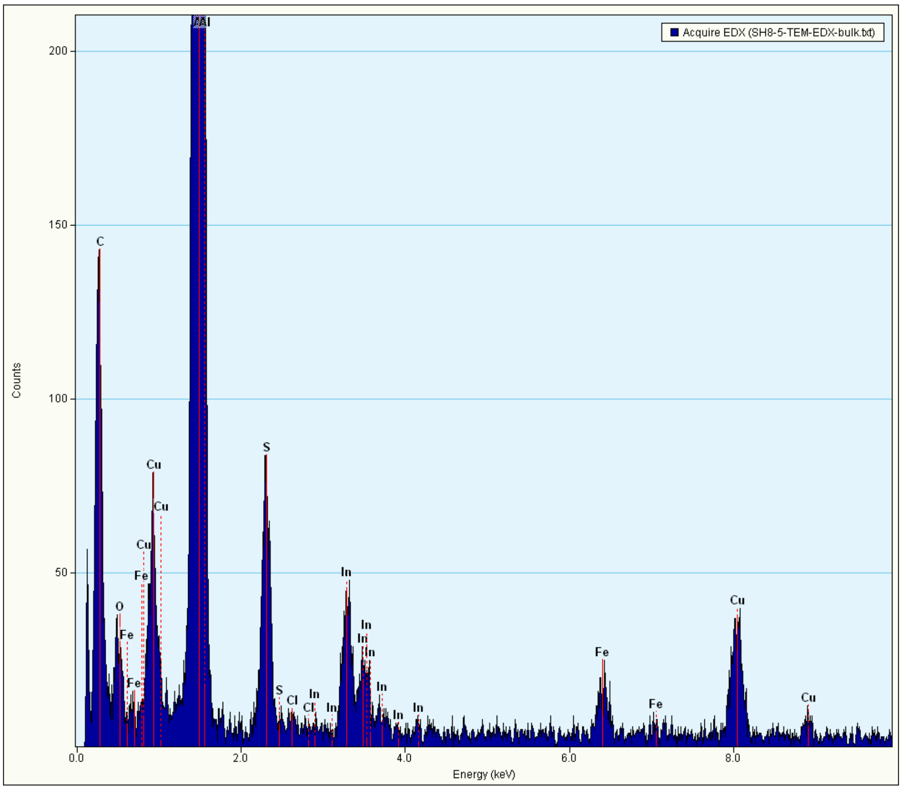

Appendix Figure 3. EDX spectrum of $CuInS_2$ nanocrystals, obtained by reacting $Cu_{2-x}S$ bifrustum parent nanocrystals with $InCl_3$-TOP at 100°C, overnight.

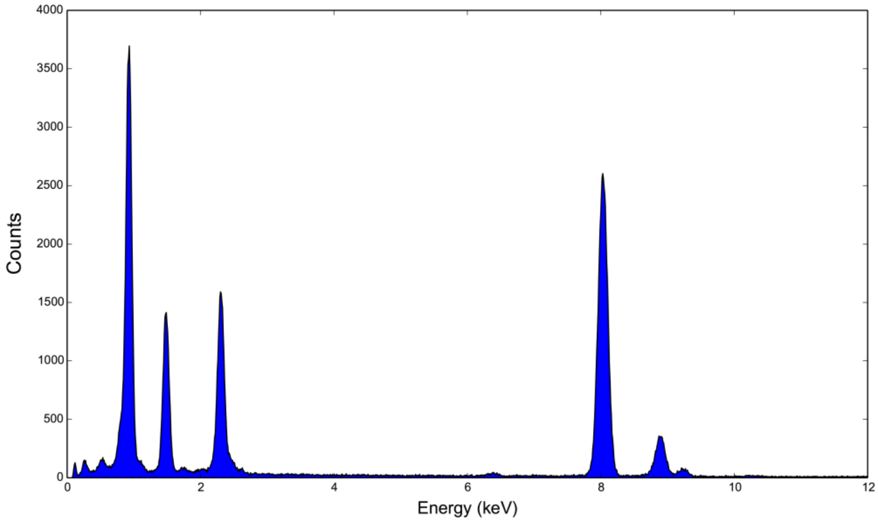

Appendix Figure 4. EDX spectrum of Cu_2S:Ga nanocrystals, obtained by reacting $Cu_{2-x}S$ bifrustum parent nanocrystals with $GaCl_3$-TOP at 100°C, overnight.

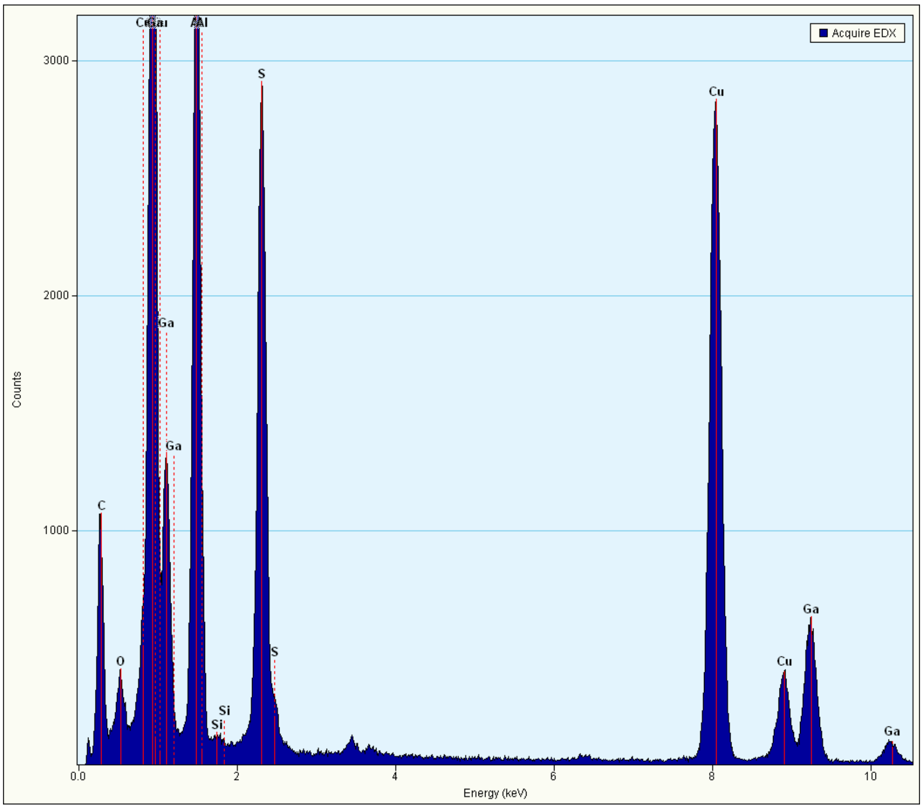

Appendix Figure 5. EDX spectrum of Cu_2S:Ga bipyramid nanocrystals, obtained by reacting $Cu_{2-x}S$ bipyramid parent nanocrystals with $GaCl_3$-TOP at 200°C, overnight.

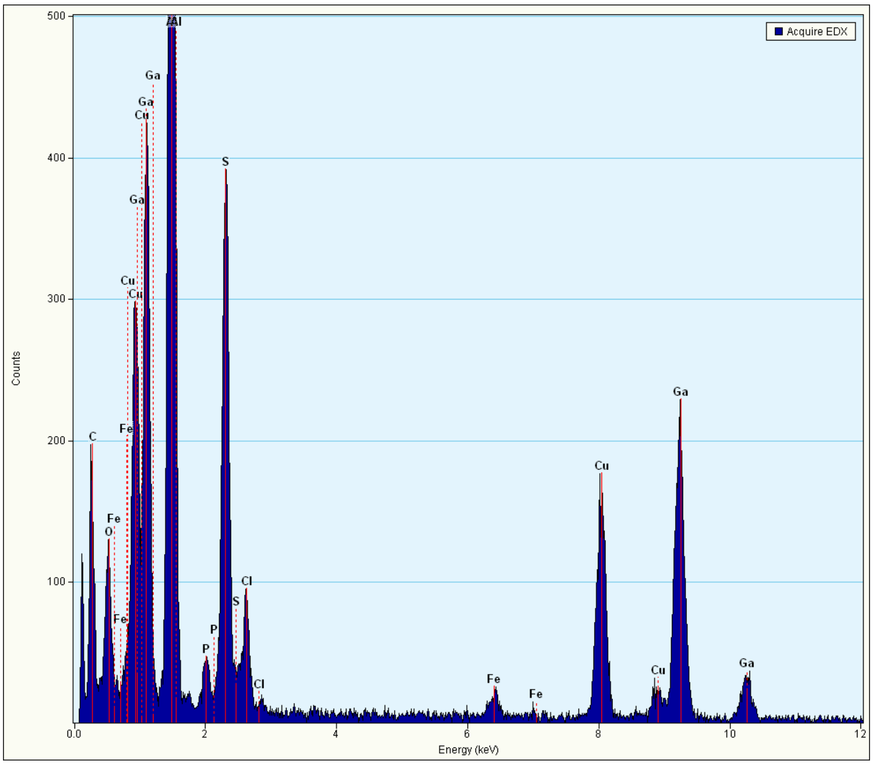

Appendix Figure 6. EDX spectrum of $CuGaS_2$ nanoparticles, obtained by reacting $Cu_{2-x}S$ bifrustum parent nanocrystals with $GaCl_3$-DPP at 100°C, for 60 min.

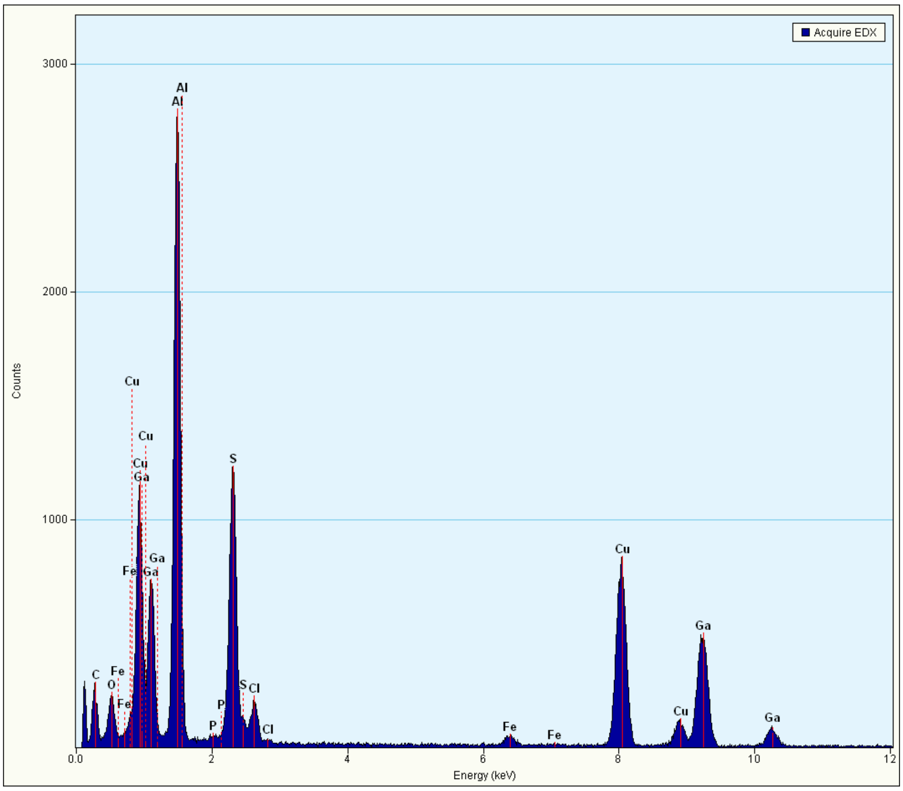

Appendix Figure 7. EDX spectrum of $CuGaS_2$ nanocrystals, obtained by reacting $Cu_{2-x}S$ bifrustum parent nanocrystals with $GaCl_3$-TPP at 100°C, for 60 min.

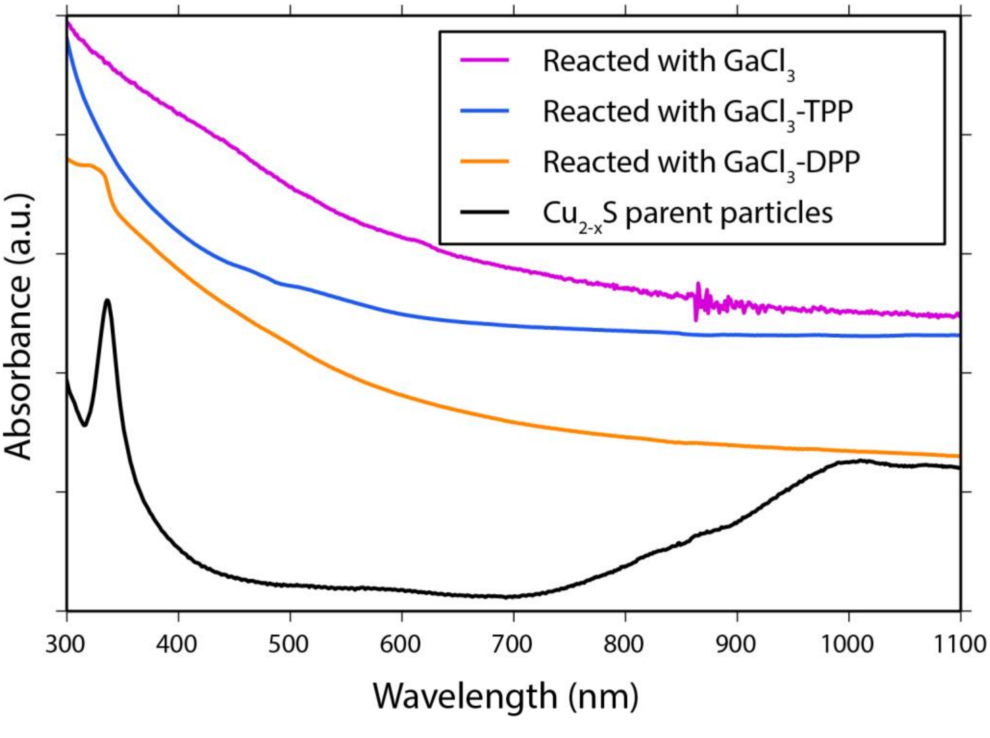

Appendix Figure 8.Absorbance spectra of (bottom, black) $Cu_{2-x}S$ bifrustum nanocrystals; (second from bottom, orange) $CuGaS_2$ nanoparticles, obtained by reaction with $GaCl_3$-DPP at 100°C, for 60 min; (second highest, blue) $CuGaS_2$ nanocrystals, obtained by reaction with $GaCl_3$-TPP at 100°C, for 60 min; (top, pink) Cu_2S/$CuGaS_2$ nanocrystals, obtained by reaction with $GaCl_3$ at 30°C, for 120 min.

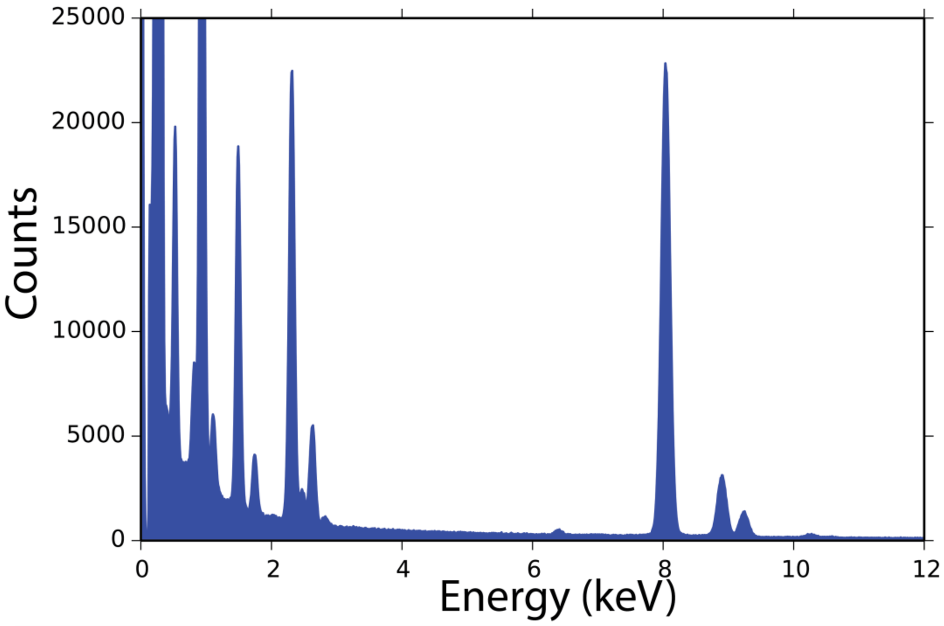

Appendix Figure 9. EDX spectrum of nanoparticles obtained by reacting bifrustum $Cu_{2-x}S$ parent nanocrystals with $GaCl_3$, at 30°C, for 120 min.

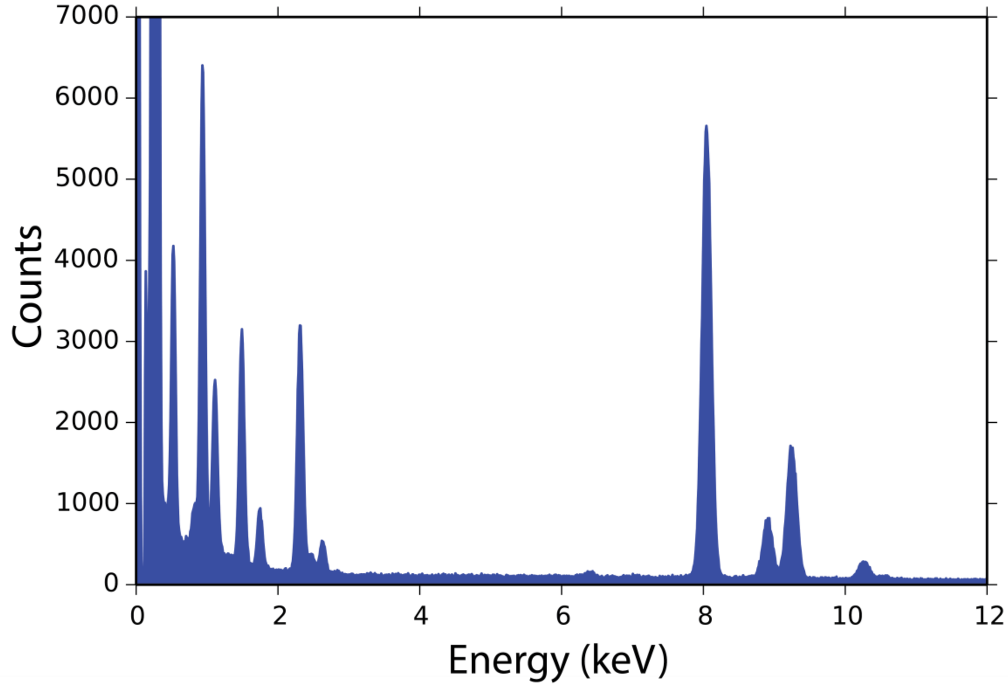

Appendix Figure 10. EDX spectrum of nanoparticles obtained by reacting bifrustum $Cu_{2-x}S$ parent nanocrystals with $GaCl_3$, at 30°C, for 300 min.

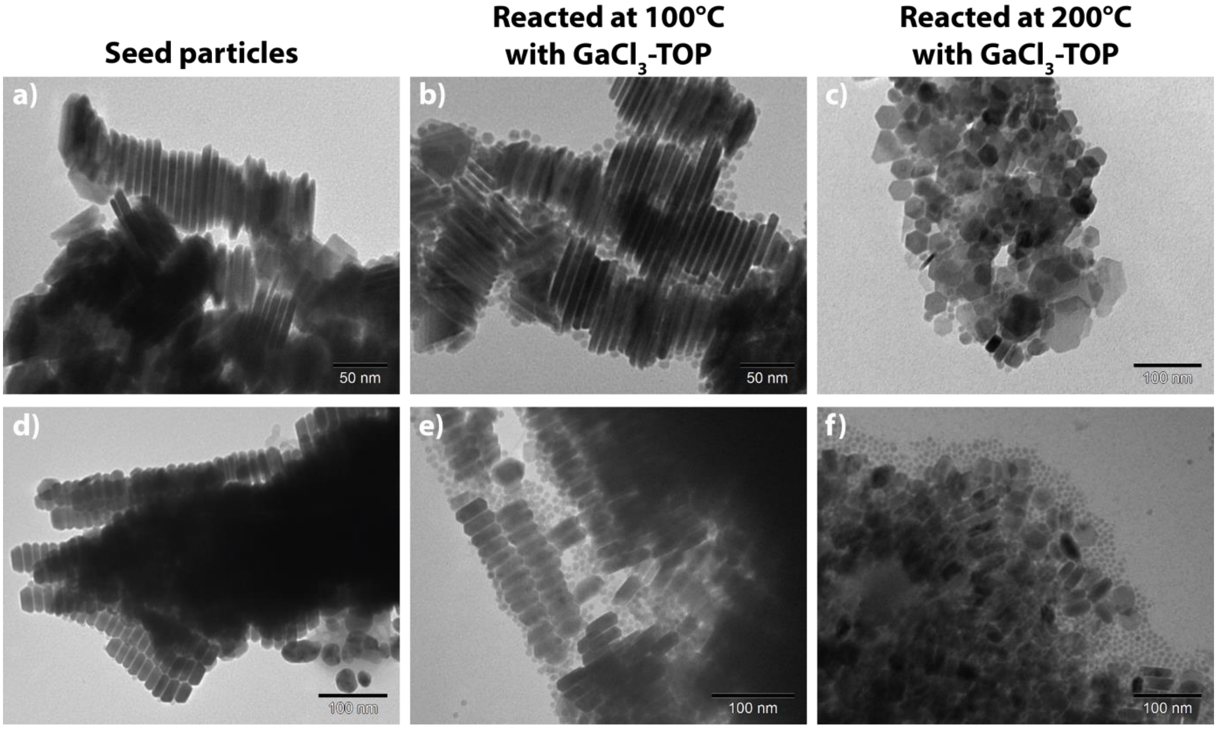
Seed particles
Reacted at 100°C with GaCl$_3$-TOP
Reacted at 200°C with GaCl$_3$-TOP
a)
50 nm
b)
50 nm
c)
100 nm
d)
100 nm
e)
100 nm
f)
100 nm

Appendix Figure 11. TEM micrographs of two types of $Cu_{2-x}S$ nanoplatelets. (a,d) before reaction; (b,e) after reaction with $GaCl_3$-TOP at 100°C; (c,f) after reaction with $GaCl_3$-TOP at 200°C.

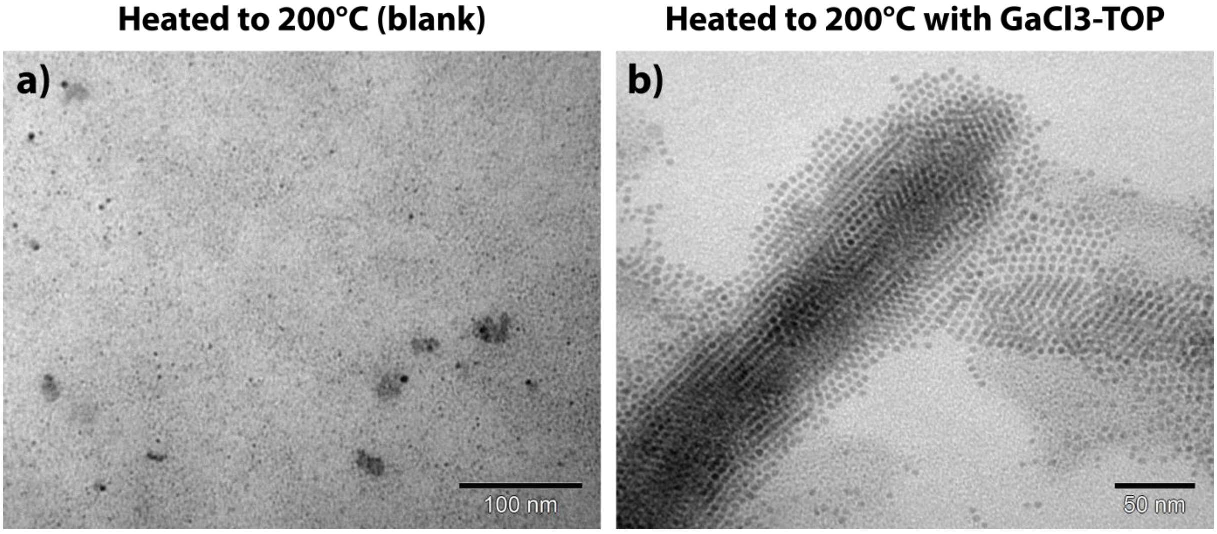
Heated to 200°C (blank)
Heated to 200°C with GaCl3-TOP
a)
100 nm
b)
50 nm

Appendix Figure 12. TEM micrographs of small sphere-like $Cu_{2-x}S$ nanocrystals (a) heated to 200°C, overnight; (b) heated to 200°C with $GaCl_3$-TOP.